as the case with a VBL, suggests that a composite VBL which contains a BP can also be observed optically though it may be difficult to distinguish a composite VBL from a simple VBL.

Chapter 4

Cross-Tie Wall in Thin Permalloy Films

In the preceding chapter, the magnetization distribution within and around the domain wall are calculated for thin films whose magnetization was small and directed perpendicular to the film plane. This chapter presents the detailed magnetization structure of the cross-tie wall in a thin Permalloy film whose magnetization is large and therefore lies mostly in the film plane. The cross-tie wall is considered as a demagnetized Néel wall in which long-range magnetostatic interactions plays an important role. This means that the size of the computing region will affect the calculation results seriously. Thus its direct calculation would be a challenge to those who are interested in computational micromagnetics.

4.1 Preliminary

The material parameters used in this chapter are the same as those used in the section 2.5 except for the damping constant α, which is fixed at unity. The easy axis of magnetization is taken in the y-direction. The two-component system of LLG equations which is based on Cartesian component representation of the magnetization and discretized according to the backward-difference method is solved using the ILUCGS method [56].

We started at small-scale two-dimensional planar calculations for a small rectangular film to test the feasibility of the calculation of the cross-tie wall. The cross-tie wall appears in the film-thickness region where the energy of the Bloch wall becomes almost equal to that of the Néel wall [36]. According to the theoretical prediction ([37]), the cross-tie wall in Permalloy film appears in a film with thickness ranging from 20 nm to 90 nm. Since the width of Néel wall increases as the film thickness decreases, a thicker film is desirable for this test calculation using the small calculation region. Thus the thickness of the Permalloy film is chosen to be 50 nm. Figures 4.1(a) and 4.1(b), in which the orientation of the magnetization in each of the computing cells is represented by a three-dimensional top, illustrate the initial magnetization configurations used in this section. In the "circular" configuration shown in Fig. 4.1(b), the in-plane component of $\boldsymbol{M}$ is aligned concentrically around the center of the computing region. The film-thickness component of $\boldsymbol{M}$, M_z, is given by

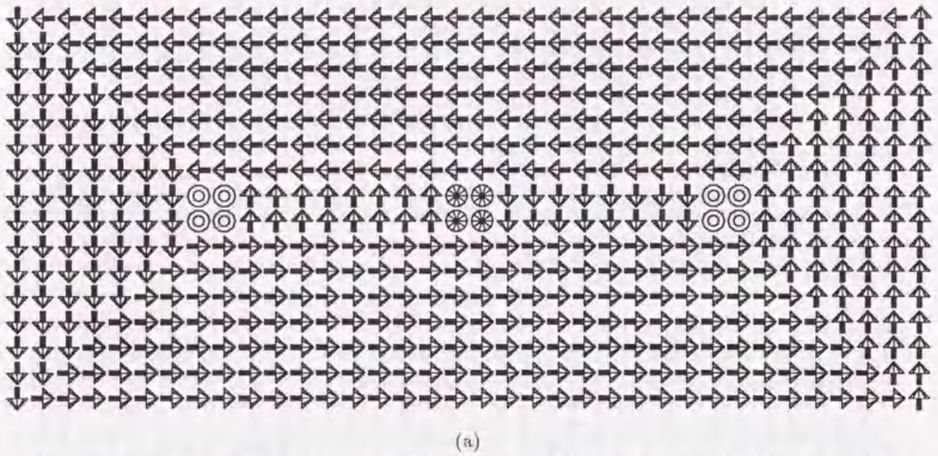

(a)

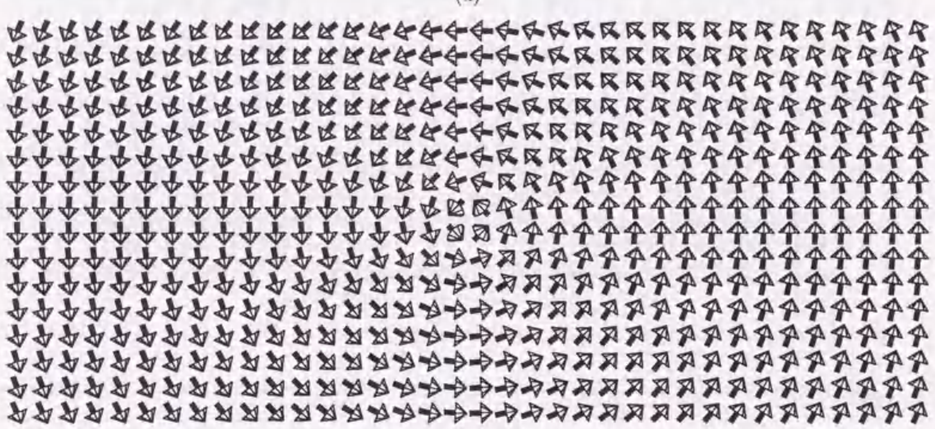

(b)

Figure 4.1: Initial states used for planar 2D calculation. (a) "step" and (b) "circular". Parameters used are: n_x=16, n_y=36 and $\delta x = \delta y$ = 8nm.

$$M_z(r) = \cos\left(\theta(r)\right),$$

with

$$\theta(r) = 2\tan^{-1}\left(\exp\frac{4r}{\sqrt{A/2\pi M^2}}\right) - \frac{\pi}{2},$$

where r is the distance from the center.

The equilibrium states derived from the "step" and "circular" initial states are shown in Figs. 4.2(a) and (b), respectively. The geometric parameters are the same for both calculations: $\delta x = \delta y = 8$ nm, $h = 50$ nm, $n_x = 16$ and $n_y = 36$. Both equilibrium states represent flux closure structures defined by a 180° main wall and four 90° Néel walls. The main wall consists of three Bloch-wall sections separated by intermediate sections with a structure something like short Néel wall. The equilibrium configurations of Figs. 4.2(a) and (b) are almost the same in the inplane magnetization. However, they differ in the film-normal component of magnetization of the three Bloch-wall sections. While the magnetization of the Bloch-wall sections are in $-z$, $+z$ and $-z$ directions counting from left to right in the configuration shown in Fig. 4.2(a), they are all in $+z$ direction in Fig. 4.2(b). The total energies of these equilibrium configurations are 4.91×10^{-11}J/m^3, 5.02×10^{-11}J/m^3, respectively. The relative differences in the total energies between these two configurations are 2.19 %. Thus the configuration in Fig. 4.2(b) is considered one of the meta stable states. It seems that the initial state given by Fig. 4.1(a) is suitable for our calculation in the sense that it derives lower-energy state. But the number of the Bloch-wall section can be given arbitrarily in this kind of initial state. Because we want to obtain the natural configuration of the cross-tie wall, I wonder the initial state of Fig. 4.1(a) is always a good

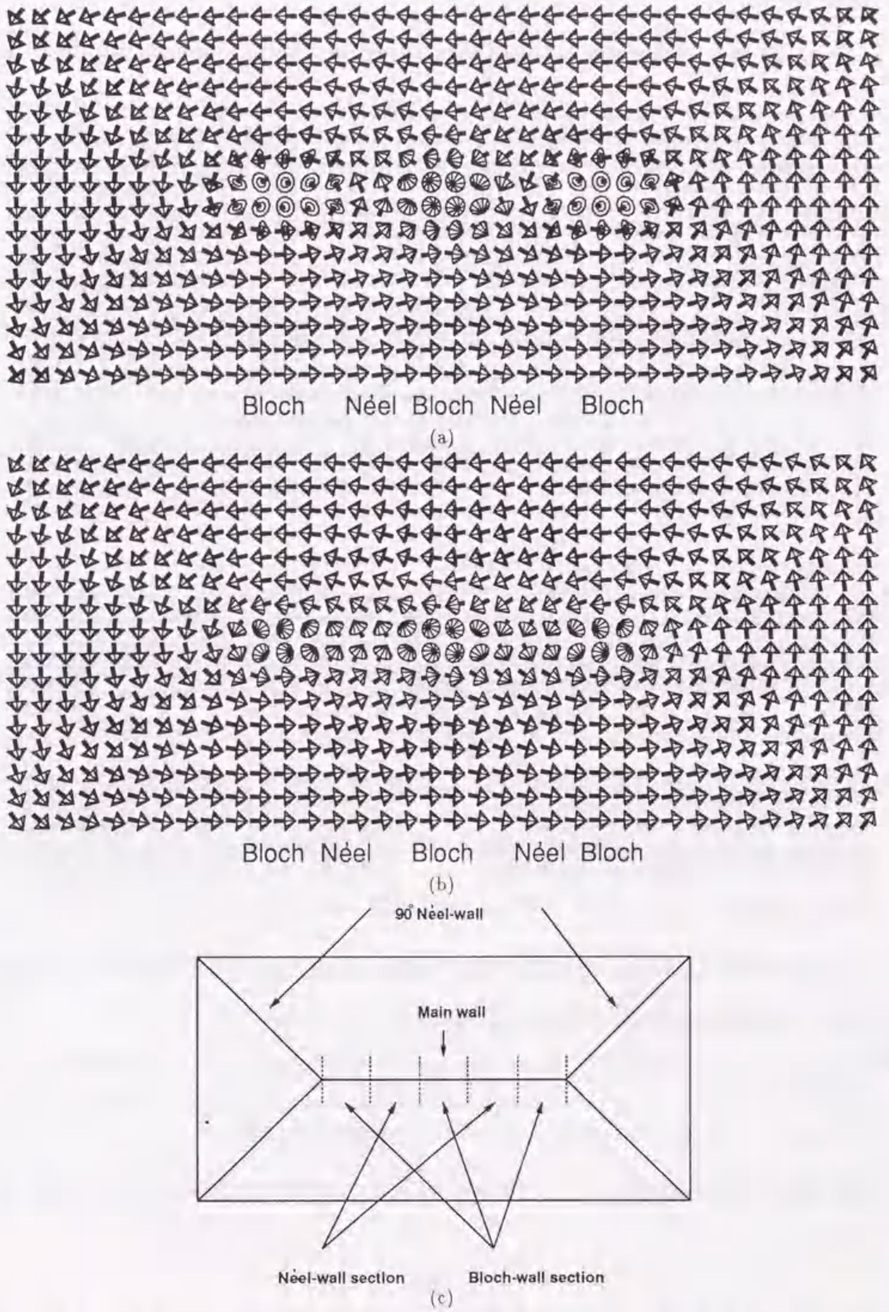

Figure 4.2: Equilibrium state of small, 50-nm-thick Permalloy film. (a) and (b) show the configurations derived from the "step" and "circular" state, respectively.

initial state.

The time step used in the calculations starting from both "circular" and "step" states is 0.02 ns. The numbers of calculation step are 495 and 577 in the respective cases. The rms values of the reversible torque averaged over the computing region are decreased to less than unity starting at the initial values in the order of 10^6.

Figures 4.3(a) to 4.3(d) present the result of a three-dimension calculation which is preformed to examine the validity of the two-dimensional planar calculation (Fig. 4.2(a)). The thickness h of the film (50 nm) is further divided into five: $n_x = 16$, $n_y = 36$, $n_z = 5$, $\delta x = \delta y = 8$ nm and $\delta z = 10$ nm. The initial state is composed of the equilibrium state derived from the two-dimensional calculation (Fig. 4.2(a)) stacked in the z-direction. The figures show the converged state obtained after 96 steps of calculation using Δt of 0.1 ns. The magnetization configuration in the midplane shown in Fig. 4.3(a) resembles the result of the two-dimensional calculation given in Fig. 4.2(a). Figures 4.3 and (b), (c), (d) show the magnetization configuration in the planes perpendicular to the film surface. From these figures, we can see that the variation of the magnetization in z-direction is relatively small.

Figure 4.3(b) shows the cross sectional view of the magnetization configuration in the xz plane containing the center of the main wall. The regions where magnetization is pointing up- or downward are the Bloch wall sections, and the regions with magnetization in parallel with $\pm y$-direction are the Néel wall sections as indicated.

Figure 4.3(c) shows the cross sectional view in the xz plane containing Néel wall section. We can observe slight variation in the magnetization along the film normal. This is considered to be the so-called asymmetric Néel wall. Because of the small size of the calculation

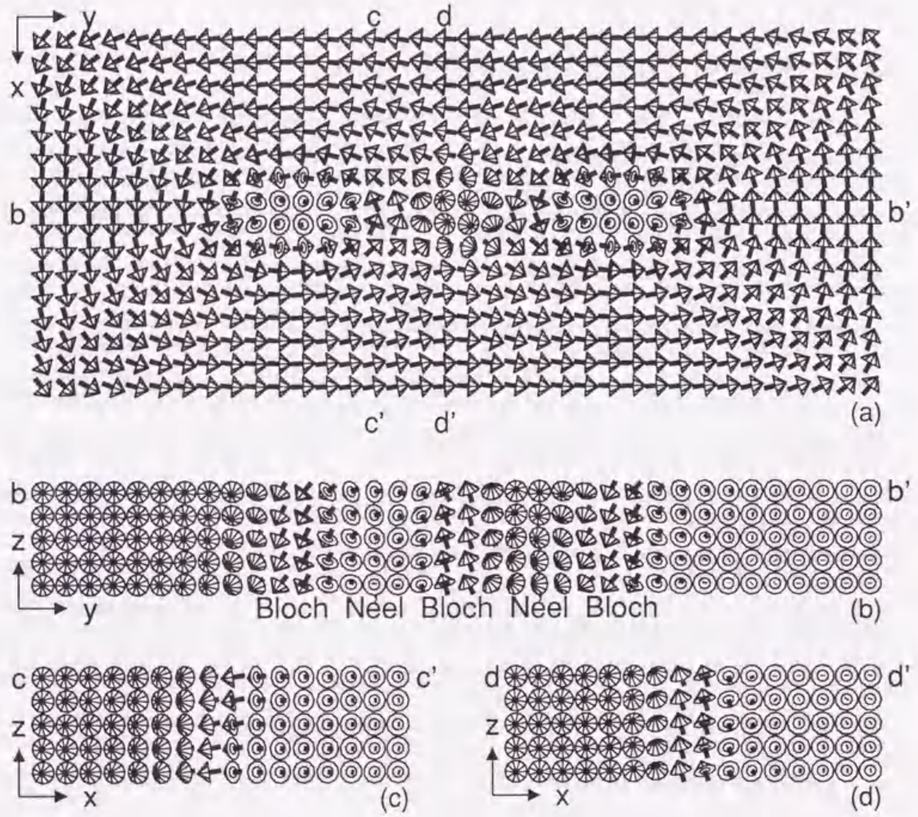

Figure 4.3: Magnetization configuration of cross-tie wall obtained by three dimensional calculation. (a) Cross sectional view of mid plane. (b) Cross sectional view of main wall along b-b'. (c) Cross sectional view of Néel section across the main wall (along c-c'). (d) Cross sectional view of Bloch section across the main wall (along d-d'). The number of division in the z direction was five (n_z=5). Δt of 0.1 ns was used.

region, the asymmetry in the magnetization structure is not so clear.

Figure 4.3(d) shows the xz plane which contains the Bloch wall section.

4.2 Structure of Cross-Tie Wall

We performed planar two-dimensional calculations with extended computing region in order to search for the equilibrium configuration of the cross-tie wall. The thickness of the Permalloy film was chosen to be 35 nm where the energy of the Bloch wall balances the energy of the Néel wall [37]. In the preceding section, we observed that the magnetization configuration in the midplane of a 50-nm thick Permalloy film was almost the same as that derived from the two-dimensional calculation. Judging from this result, we can expect that the results of planar two-dimensional calculations would reproduce the magnetization configuration in the midplane for a Permalloy film of this thickness.

In order to extend the computing region for the cross-tie wall as large as possible, we eliminated the closure domains at the boundaries in the y-direction by employing the periodic boundary condition in this direction. This enabled us to calculate the structure of a cross-tie wall with the period equal to the size of the computing region in y-direction. The source region of the demagnetizing field was extended by a hundred period on both sides of the computing region (λ=100, see subsection 2.2.2).

The numbers of divisions in y direction were fixed at 120. The numbers of divisions in x direction were varied from 120 to 600. The mesh size was fixed at 8 nm. When we use larger mesh size, the magnetization structure around a Bloch line can not be reproduced correctly due to the discretization error. In the case with n_x= n_y= 120, the demagnetizing

field was calculated using every element cell in the computing region. In the other cases with larger n_x, source cells distant from the observing cell were treated in blocks of 5×5 element cells. It was confirmed that the error in the orientation of $\boldsymbol{M}$ in the equilibrium state for 120×120 meshes, when the latter method was used, was less than 1 degree almost everywhere in the computing region except in the vicinity of the Bloch lines where the orientation error was about 5 degrees. In the case of the rigorous calculation with 120×120 cells it took 694 steps of calculation using a time step of 0.02 ns until the rms value of the reversible torque decreased below unity from the initial value of about 10^6. The total computing time was about one hour when a HITAC S-820/80 was used. A variation of the "circular" state with elliptical streamlines was used as the initial state.

In Figs. 4.4(a) to 4.4(c), the detailed magnetization structure of cross-tie wall calculated is compared with the interference image taken by electron holography [39]. In-plane magnetization directions at every fifth cell are shown in (a) over two periods. The magnetization direction was processed to construct the streamlines which is shown in Fig. 4.4(b). Although the overall dimensions are not exactly the same, the streamlines derived from the calculated magnetization configuration are seen to agree well with the observed image of interference microscopy.

It should be noted that the period of the cross-ties is fixed at 960 nm in the present calculation. This means that the equilibrium state shown in Figs. 4.4(a) represents an energy minimum under the constraint of a fixed cross-tie period. The period which gives the true energy minimum should be determined by using different cross-tie period. These calculations, however, will be made when a more effective method is established to reduce

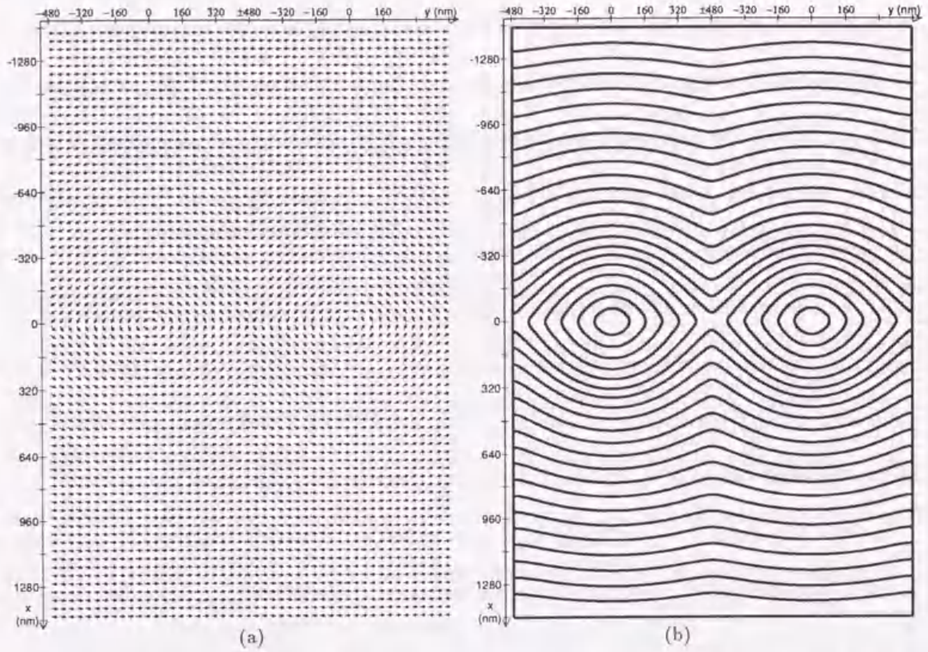

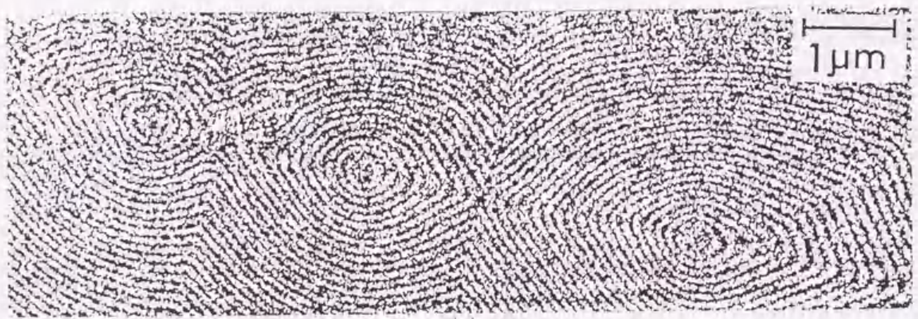

Figure 4.4: Magnetization configuration of cross-tie wall in Permalloy film. (a) The direct result of simulation. (b) The stream lines derived from (a). (c) The image of cross-tie wall observed by interference microscopy of electron holography [39]. The parameters used in the simulation are: n_x=600, n_y=120, $\delta x = \delta y = 8$ nm (960 nm period) and Δt=0.02 ns. The magnetization vectors at every fifth cell are shown in (a). The display area is 2.88μm in the central portion in x-direction and two periods in y-direction.

the cost of computation.

Next, we would like to discuss on the effect of calculation region in x-direction.

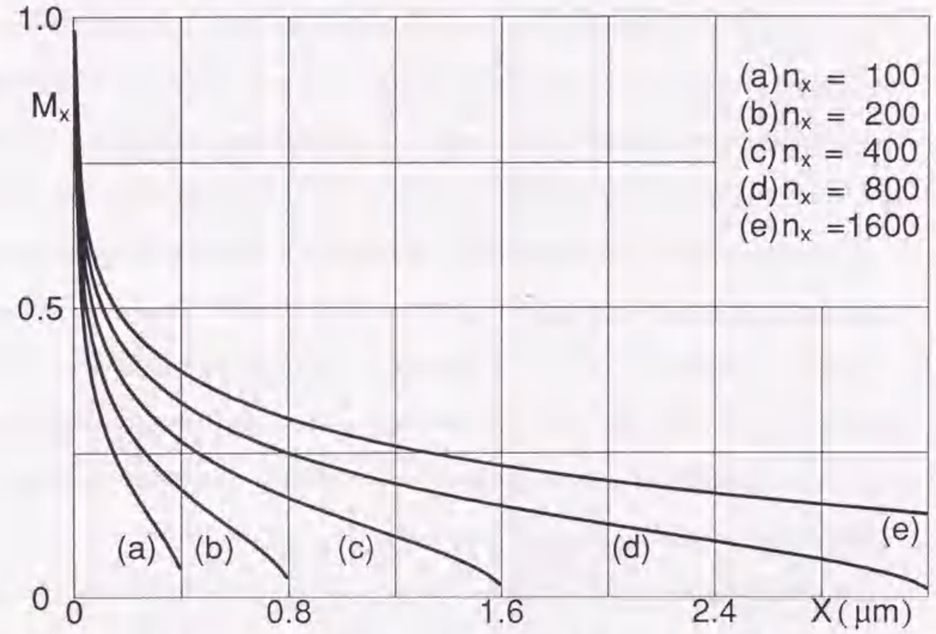

Figure 4.5: Effect of computing region on magnetization structure of Néel wall. The wall-normal component M_x calculated using different value of n_x is plotted against distance x from wall center.

Figure 4.5 shows the wall-normal component of the magnetization in the one-dimension Néel wall as a function of the distance from the wall center. The results were derived from different sizes of computing region using the same material parameters as uses in the calculation of the cross-tie wall. The Néel wall is said have a long tail extending widely from the core of the wall [37]. This feature of the Néel wall can be seen in this figure. The rotation angle 60° of magnetization from the wall tangent corresponds to the wall-normal

component $M_x = 0.5$. When half the computing region in the x direction is 1.6 μm long (case (c) in Fig. 4.5), M_x reaches this value at a distance of 0.1 μm from the wall center. The portion of the wall where $M_x > 0.5$ and the other portions which extend outside the former may be regarded as the core and the tail of the wall, respectively. Figure 4.5 clearly shows that the tail portion of the Néel wall is not only long but also its length depends on the width of the computing region. M_x does not reach zero sufficiently even at the boundary of the computing region. The cross-tie wall, which can be regarded as consisting of sections of Néel walls with opposite polarities of M_x repeated periodically in the y direction, is considered to inherit the characteristics of having long tails associated with the Néel wall. Therefore the result of calculation derived from a finite computing region may not represent the structure of the actual cross-tie wall in a film whose dimension is infinite in the direction perpendicular to the wall.

In Figs. 4.6(a) and 4.6(b), the streamlines of the planar magnetization calculated derived from smaller n_x are compared with those shown in Fig. 4.4(b) derived from n_x= 600. Although the set of the streamlines obtained using n_x= 120 differs considerably from that obtained using n_x= 600, the lines for n_x= 240 coincide well with the lines derived from n_x= 600 in the region where the lines are drawn solid.

So far, we discussed the effect of the size of the computing region on the configuration of the cross-tie wall calculated. The discussion may be summarized as follows. In spite of the use of a finite computing region, the configuration of the calculated cross-tie wall can be regarded to approximate the one in the infinite medium except for portions near the boundaries of the computing region when n_y is 120 and n_x is greater than ~240.

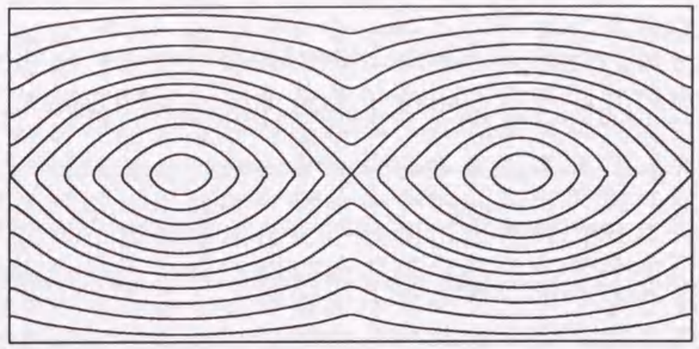

(a)

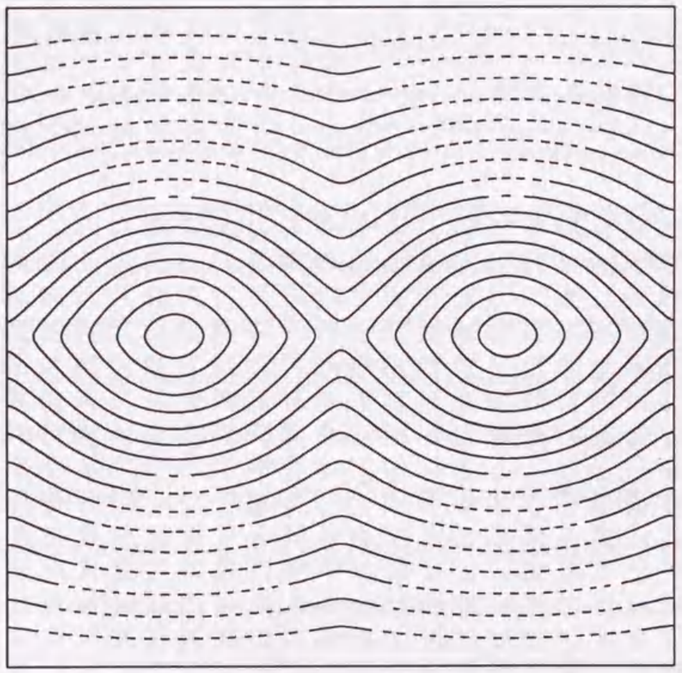

(b)

Figure 4.6: Effect of computing region on magnetization structure of cross-tie wall. The cases with (a) n_x=120 and (b) n_x=240 are compared with the result derived from n_x=600 shown in Fig. 4.4(b).

Figures 4.7(a) and 4.7(b) show the details of the cross-tie wall around Bloch lines of circulation and contracirculation type, respectively, where n_x= 210 and n_y= 120. Detailed structure of the main wall portion between two neighboring Bloch lines is shown in Fig. 4.7(c) taking the result of a small-scale calculation derived from n_x= n_y= 40 as an example. The magnetization of every element cell is represented by a three-dimensional top. These figures show that the conceptual structure of the cross-tie wall we have imagined [37] is actually an energy-minimal state derived from a first-principle calculation in which nothing is assumed essentially except for the material and geometric parameters.

The distributions of energy components associated with the cross-tie wall are revealed in Figs. 4.8(a) to 4.8(e), which show the contour lines of various energy densities derived from the equilibrium configuration shown in Figs. 4.4(a) and 4.4(b). The contour lines of total, exchange, anisotropy and magnetostatic energy densities are shown in the respective figures (a) to (d) of Fig. 4.8. The spurious sawtoothlike undulations appearing on the contours for negative values of ε in Fig. 4.8(a) are considered to be due to the above-mentioned time-saving calculation of the demagnetizing field because contour lines are always smooth in the energy distributions derived from small-scale calculations in which the contribution of every cell is properly taken into account. In order to smooth out the contour lines by removing the undulate, ε is averaged over the block of 5×5 cells centered at the observing cell, and the result is shown in Fig. 4.8(e). Because the contours of the magnetostatic energy density ε^D are similarly undulating, they are also smoothed out in Fig. 4.8(d). On the other hand, the undulations were not observed in the contours of the anisotropy energy density ε^K as shown in Fig. 4.8(c). The contours of the exchange energy ε^A shown in Fig. 4.8(b) are

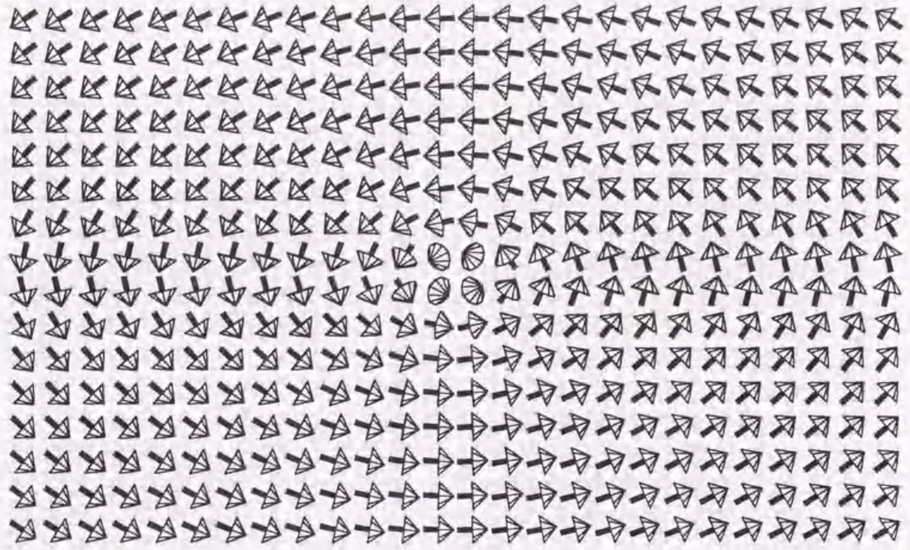

(a)

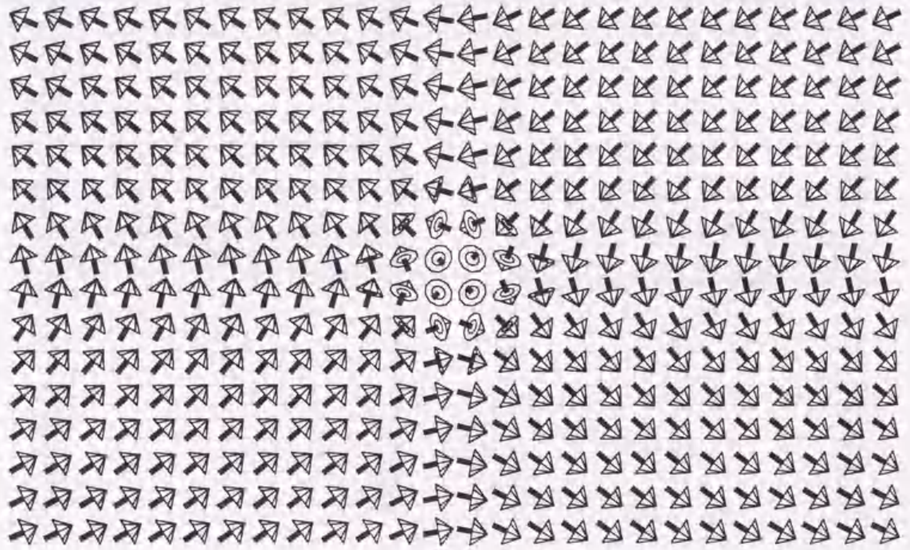

(b)

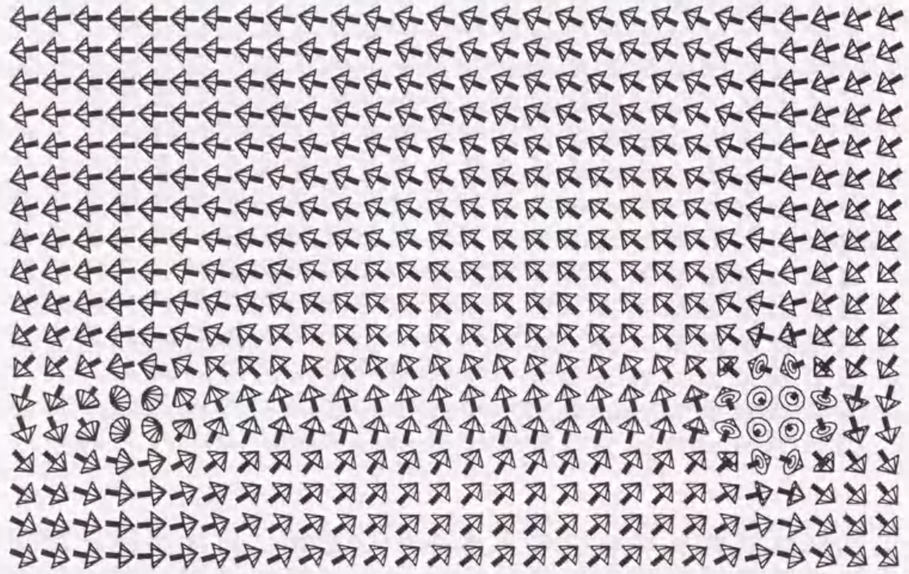

(c)

Figure 4.7: Details of cross-tie wall (portion). The magnetization vectors at every cell are shown. The all of the calculation regions are n_x=210, n_y=120 and n_x=40, n_y=40 in (a and b) and (c), respectively. (a) Neighborhood of a circulating Bloch line. (b) Neighborhood of a contracirculating Bloch line. (c) Close-up of the main wall between the two types of the Bloch lines.

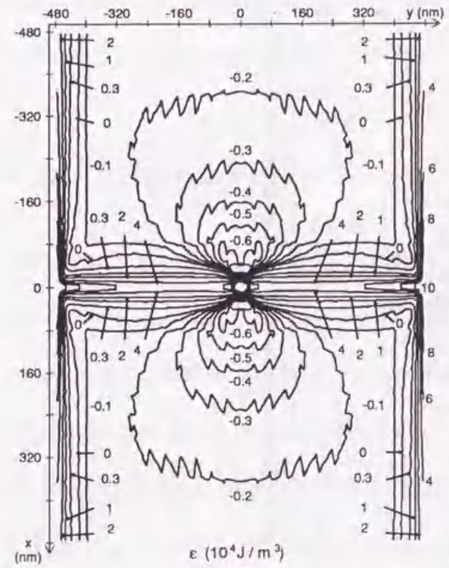

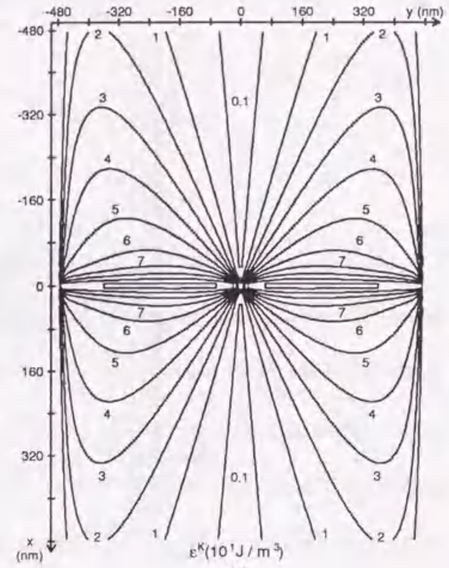

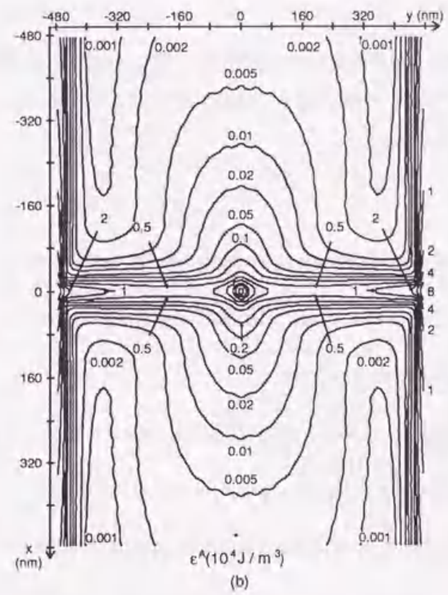

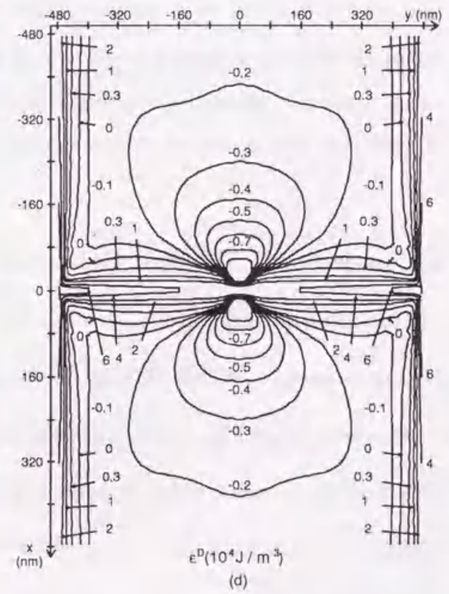

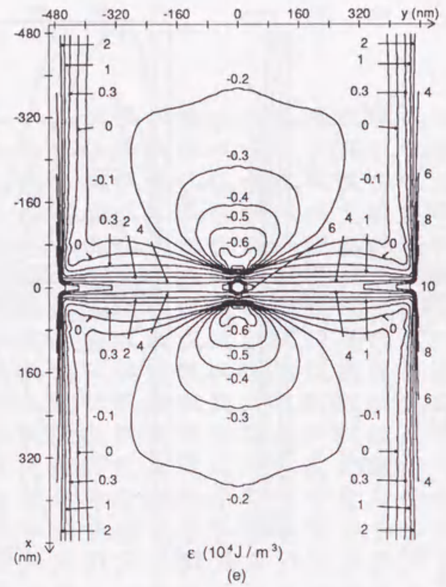

Figure 4.8: Energy distributions around cross-tie wall. (a) and (e) Total energy density ε. (b) Exchange energy density ε^{A}. (c) Anisotropy energy density ε^{K}. (d) Magnetostatic energy density ε^{D}. The energy densities were averaged in block of 5×5 cells in (d) and (e).

not smoothed out. The slight tendency toward undulation is considered to be due to the differentiations which enhance small undulation of the magnetization components induced by the magnetostatic field through the equilibration process.

As shown from Fig. 4.8(e), the wall energy is stored essentially in narrow regions of about 40 nm in width which extend along the main wall and cross-ties. The wall energy is highly concentrated in the vicinity of the Bloch lines with the radius of about 20 nm. The exchange and magnetostatic energy densities account for most of the wall energy density

and the anisotropy energy is small compared with these energies in the case of Permalloy, because K_u is very small in this material.

4.3 Summary

Detailed magnetization configuration of cross-tie wall in a thin Permalloy film are obtained using the numerical method developed in this thesis, implicit solution of the LLG equation expressed in Cartesian components of magnetization. In order that the result of the calculation could be compared with experiment, the size of the computing region is made as large as possible (0.96 μm in the direction of the main wall and 4.8 μm in the wall-normal direction) within the limit of the budget. The derived structure resembles very closely with the interference image of a cross-tie wall taken by electron holography, which shows the validity and effectiveness of the developed numerical method.

Chapter 5

Magnetization Reversal in Cubic Particles

The magnetization state and the reversal mechanisms in fine ferromagnetic particles of spheroidal shapes were investigated firstly in 1960's using analytic methods [1]. Recently, the numerical method has been popular in order to investigate the magnetization reversal mechanism of fine particles with various shape [6, 7, 8, 9, 10, 11]. However, most of these calculations are static calculations based on the Brown's equation. In this chapter, the magnetization reversal mechanisms in fine cubic particles are investigated based not only on the quasistatic calculation but also on the dynamic calculation by solving LLG equation.

The magnetization configurations of cubic particles were studied by Schabes and Bertram (SB)[7]. They found that there exist flower and vortex states in the absence of applied field; the flower state stable for small particles and the vortex state stable for large particles. They also found that magnetization reverses coherently from the flower state while a more

complex reversal mechanism occurs from the vortex state. Because their calculations are based on the quasistatic method of finding the energy minimum state, it is impossible to determine the time-dependent properties of magnetization change. On the other hand, the calculation methods proposed in this thesis are based on the LLG equation, and therefore we can examine the dynamical reversal process of magnetization.

In section 5.2, the remanent magnetization states of cubic particles with different sizes are calculated and compared with the results of SB. It is found that there is a range of particle size in which both flower and vortex states are stable. In the remainder of the chapter, sections 5.3 $\sim$ 5.6, various types of the magnetization reversal processes are studied in detail.

5.1 Preliminary

The material parameters of a typical magnetic oxide (γ-Fe_2O_3) are used in the calculation except for the damping constant, M_s=0.46 T (370 emu/cm^3), $A = 0.5 \times 10^{-11}$ J/m (0.5×10^{-6} erg/cm), K_u= 1.85×10^3 J/m^3 (1.85×10^4 erg/cm^3), $\gamma = -2.21\times10^5$ rad/(s·A/m) (-1.76×10^7 rad/(s·Oe)), and α (damping constant)=1. These parameters, except α and A, are the same as for SB. The reported damping constant α of a magnetic oxide [57, 58] is much less than unity. This high α value is used to decrease the computation time (see Fig. 5.12). The exchange constant A in SB is 1.0×10^{-11} J/m (1.0×10^{-6} erg/cm) but this should be read as being half of it.[1] The easy axis is in the z-direction. The cubic particles are divided into cells of $5 \times 5 \times 5$ regardless of the particle size. The sizes of the cells are

[1] M. E. Schabes: private communication.

thus changed from 4 to 15 nm. That is, the sizes of the particles are between 20 and 75 nm. The size of each cell in the x direction, δx, is always the same as δy and δz.

Unlike the quasi-static calculations performed in chapter 4, the calculations in this section aim at pursuing magnetization changes with time as accurately as possible at the expense of computation time. Thus considerably small time steps (smaller than $\sim$1 ps) are used for the sake of accuracy, though the stability limit Δt_u is greater than 0.1 ns when the backward difference method is used. Δt_u is observed between 2 and 5 ps when the conventional forward-difference method is used for typical equilibration calculations made in this section. This means that the conventional explicit method can also be used in this particular application though we used the backward difference method.

5.2 Equilibrium States

According to SB, there are two kinds of remanent states depending on the size of the particles, which are named flower and vortex states. The flower state appears in small particles while the vortex in large ones. Figure 5.1 illustrates these two states. The directions of the magnetic moments are shown by the tops. This figure aids understanding of the origins of the words flower and vortex. The effect of particle size on average magnetization in the z direction (easy axis), $\overline{M}_z$ normalized by M_s, is shown in Fig. 5.2. To check the effect of the initial state on the finally obtained equilibrium, we performed two sets of calculations starting from two different initial states which had been obtained in separate calculations using the particle size of 46 nm and 60 nm. Case 1 uses as the initial state the magnetization distribution in the equilibrium state of a 46-nm particle, flower state,

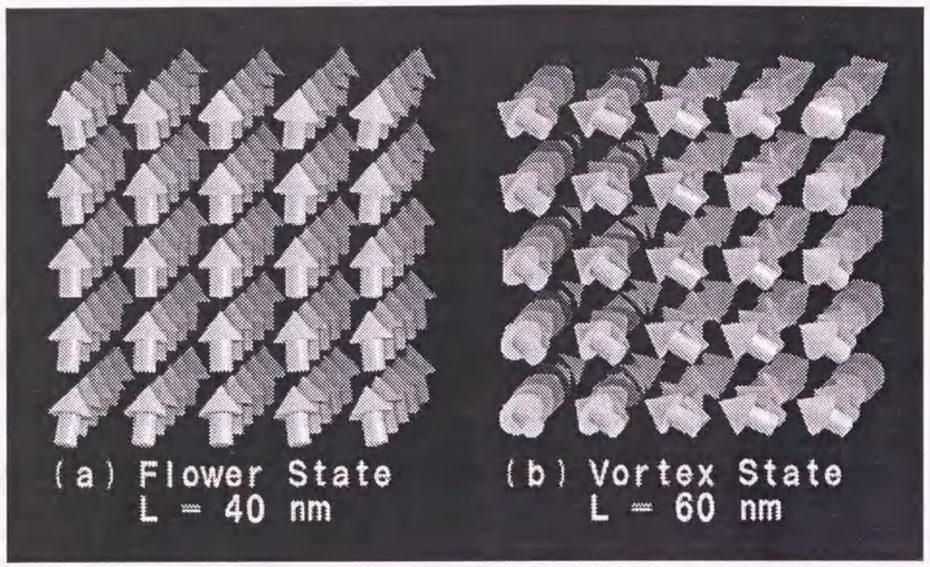

Figure 5.1: Magnetization configurations of flower and vortex states.

accommodated to enlarged cell size. Case 2 is derived similarly from the equilibrium state of a 60-nm particle, vortex state, with reduced cell size. (The equilibrium states of 46- and 60-nm particles were derived from the initial states with magnetization saturated in $+z$ direction.) $\overline{M}_z$ scarcely changes with increasing particle size when the particle size is small, but it decreases with increasing particle size when the particle size is larger than a critical value, 55.5 nm in case 1 and 51.0 nm in case 2. These features are the same as the results obtained by SB except for the critical value, which is 52 nm according to SB. In the present calculation, however, the critical value is found to depend on the initial state. The critical value reported by SB nearly coincides with our result of case 2.

Figure 5.2 shows that there are two different equilibrium magnetization states when the

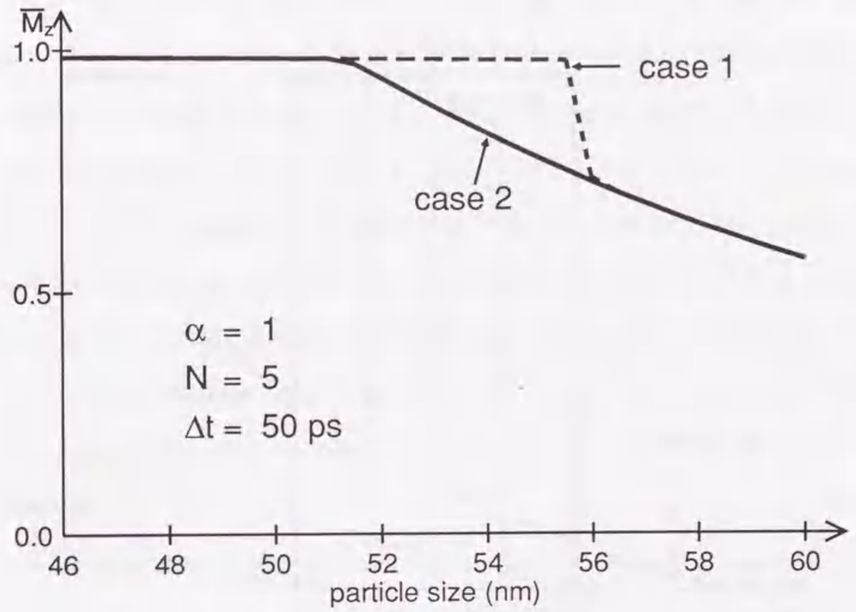

Figure 5.2: Effect of particle size L on average remanent magnetization in the z direction, $\overline{M}_z$. The results derived from two different initial states are shown. Case 1 was derived from the magnetization state of a 46-nm particle and case 2 was derived from the magnetization state of a 60-nm particle.

particle size is between 51.5 and 55.5 nm, where the magnetization state changes from the flower state to the vortex state in both of the cases. The flower state appears when the particle size is less than 54.5 nm, and the vortex state appears when the particle size is greater than that value in case 1. On the other hand the flower state appears when the particle size is less than 51.0 nm, and the vortex state appears when the particle size is greater than that value in case 2. This suggests that there are several metastable magnetization states with different energies in this particle size. To check this possibility,

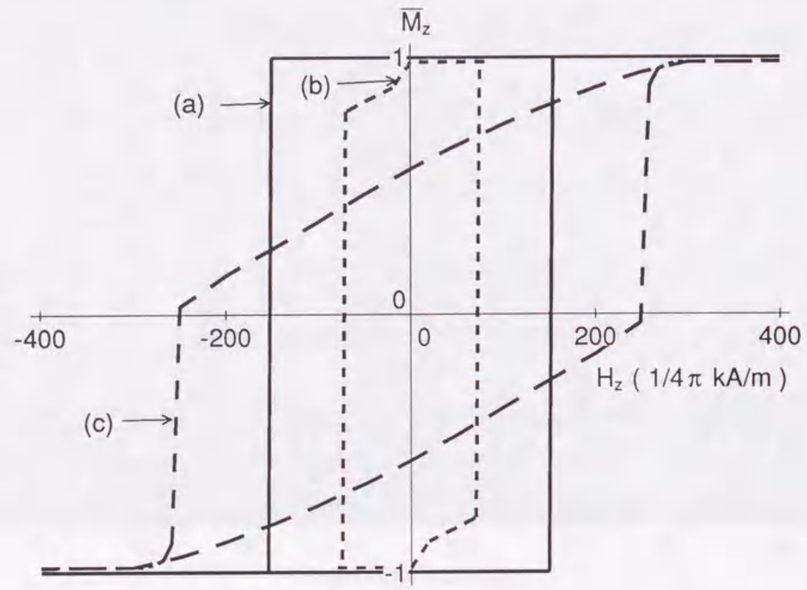

Figure 5.3: Magnetization curves of (a) 40-nm, (b) 52.5-nm and (c) 60-nm particles.

we compared the magnetic energy between the equilibrium states of both cases. The result shows that the states with smaller $\overline{M}_z$ (case 2) have smaller energy though the difference is quite small (only 2.5% in the largest case). Note that the results of the static calculations summarized in Fig. 5.2 only indicate that there are at least two stable equilibrium states when the particle size on between 51.0 nm and 54.5 nm. Because of the static nature the calculation is unable to show which equilibrium stat the particle actually possesses.

Next, we derived equilibrium states under the external field to obtain the quasi-static magnetization curves of the cubic particles with different sizes. Starting from H_z=31.8 kA/m (400 Oe), the field was varied successively at an interval of ΔH_z of 6.37 kA/m (80

Oe) so that a complete cycle of the M-H curve was obtained. At each field value the simulation was performed until the magnetization was relaxed into an equilibrium state, which was then used as the initial state in the next simulation run with H_z varied by ΔH_z. The magnetization curves for 40-nm, 52.5-nm and 60-nm particles are shown in Fig. 5.3. The $\overline{M}_z$ of a 40-nm particle is almost constant before irreversible transition, magnetization switching, occurs. It means that the magnetization state does not change significantly from the initial state before the switching occurs in this particle. But the $\overline{M}_z$ of a 52.5-nm and 60-nm particles begins to decrease before the switching. It means that there are intermediate states which are different from the initial states before the switching in these particles.

In the static calculations mentioned in the preceding paragraph, there are two kinds of equilibrium states, flower and vortex, associated with the 52.5 nm particle. The remanent state of this particle in the course of the quasi-static M-H curve is formed to be flower. Thus the equilibrium state on the curve case 1 in the static calculation is realized in this particular dynamic process, quasi static M-H loop.

The remanent state of the 40-nm particle in the M-H curve is also the flower state. We expect, however, that there may be difference between the magnetization reversal methanisms of the 40-nm and 52.5-nm particles because the latter particle has two remanent state. The results of simulation show that our prediction is correct as described in the next section. In order to distinguish between the magnetization reversal mechanisms starting at these two flower states, the magnetization state of the 40-nm particle is termed the flower1 (F1) state and that of the 52.5-nm-type particle is termed the flower2 (F2) state in this

thesis hereinafter.

5.3 Magnetization Reversal from an F1 State

In this section, the magnetization reversal process of particles in the remanent state F1 is studied. Fig. 5.4 shows the time dependence of $\overline{M}_z$ for a 40-nm cubic particle. Magnetic fields of -23.9 kA/m (-300 Oe) in the z direction and 7.96 A/m (0.1 Oe) in the x direction (offset field) are applied. It is seen in this figure that a certain time is required before an irreversible transition starts. This retardation time, τ_r, is defined as the interval between the time of field application and the time when $\overline{M}_z$ equals 0. The effect of time step, offset field and damping constant on retardation time τ_r will be discussed in the next section.

The details of magnetization reversal from an F1 state is shown in Fig. 5.5. It is seen that all moments reverse in a coherent way precessing simultaneously around the direction of the applied field. Thus the magnetization reversal mechanism is almost the same as the coherent rotation in this case.

In order to check the motions of the magnetizations before τ_r, the motions of five particular magnetic moments (at the center, and at the four corner cells in the top layer of the particle, Fig. 5.6) are examined. Figure 5.7(a) shows the changes of the azimuthal angles of these five moments. It is seen that the magnetization reverses almost coherently during switching ($t = 6 \sim 8$ ns), namely, the time dependences of the magnetization angles θ and φ are almost the same among the magnetic moments. The azimuthal angle of the moment M_{13} at the particle center decreases smoothly and monotonically throughout the simulated time. It means that the moment M_{13} continue to precess in the same direction not only

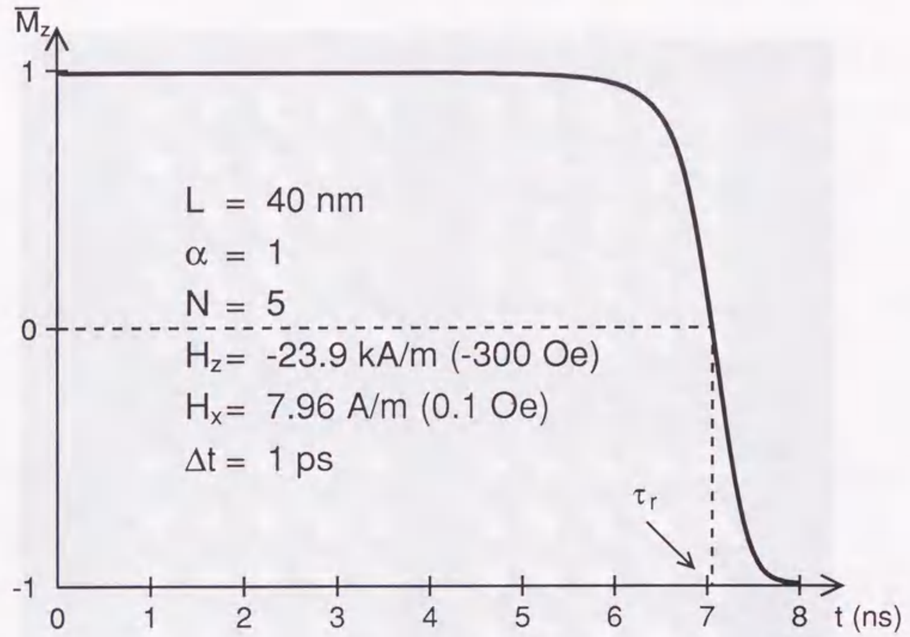

Figure 5.4: Change in $\overline{M}_z$ of flower state with time lapse t. τ_r is the time interval for the transition.

in the reversal period but also in the retardation time. But the magnetic moments at the particle corners (M_1, M_5, M_{21}, M_{25}) do not precess after the reversal, though they precess considerably in the reversal period.

Figure 5.7(b) shows the time dependence of the polar angles. The changes in the polar angles are unidirectional in the middle of the reversal period (t=6.5$\sim$8.0 ns). The polar angle of M_{13} changes smoothly and monotonically during the simulation time. But the polar angles of the other moments do not change significantly before switching, and they change in more complicated ways at the beginning of the reversal period. We can see from the figure that the z-components of the two of the corner moments , M_{21}, M_{25}, decrease

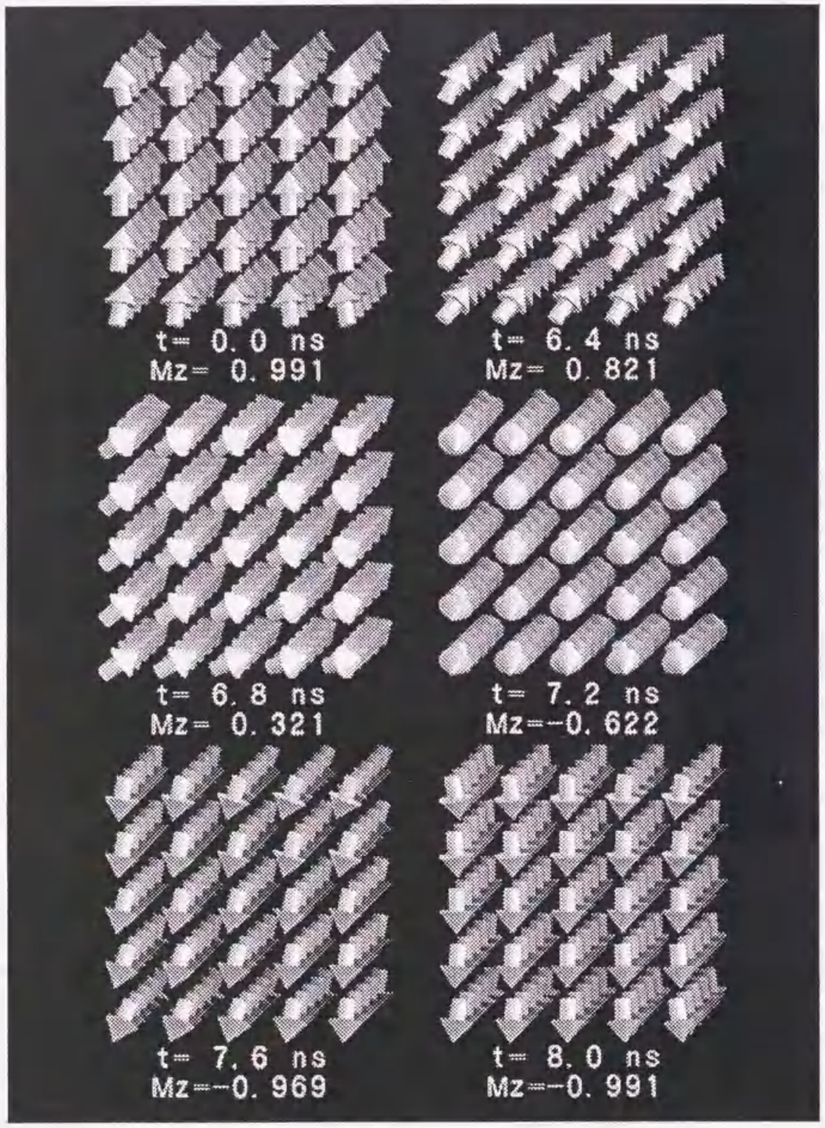

Figure 5.5: Mechanism of magnetization reversal from an F1 state.

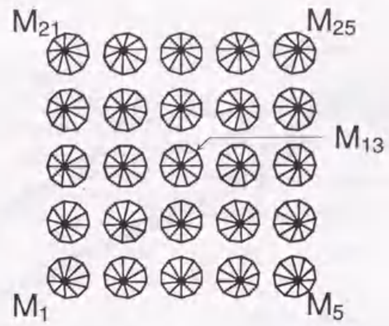

Figure 5.6: Magnetic moments in the top layer of the particle.

slightly at the beginning of the transition to reduce the demagnetizing and the Zeeman energies.

Because the polar angle of M_{13} is almost zero before the switching, the precession of M_{13} manifests itself in the change of the azimuthal angle though the amplitude of the precession is extremely small. Because the polar angles of the other moments are not zero, we cannot see the small precession of these moments from these figures. To see the motion of all the moments, we checked the angular velocity ($\dot{M}$) of the moments.

Figure 5.8 shows the angular velocity of the five moments on the top surface of the particle. The angular velocity of the center moment (M_{13}) increases almost exponentially until the end of the half magnetization reversal (t= 8.0 ns), and then decreases very quickly. The time dependence of the angular velocity of the other moments is almost the same as that of the center moment except just after the application of the external field ($t \approx 0.0$ ns). At that time, the polar angles of these moments slightly increase (Fig. 5.7(b)). It can be seen from this figure that the changes in the magnetization angles are almost the same

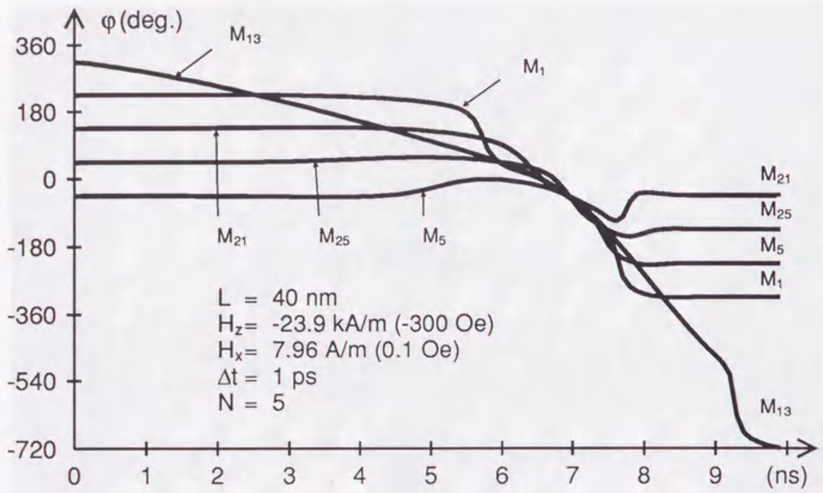

(a)

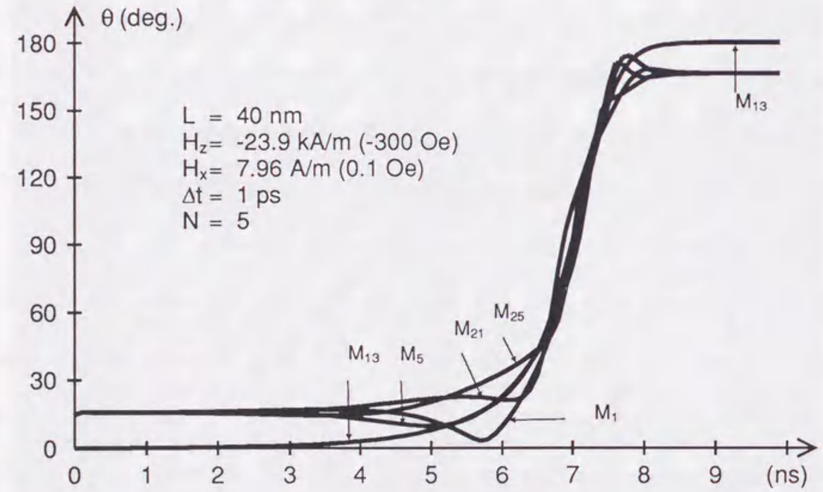

(b)

Figure 5.7: Changes in magnetic moments at five top-layer cells with time lapse t. (a) The changes in the azimuthal angles of the moments. (b) The changes in the polar angles of the moments. Switching processes derived from an F1 state are shown.

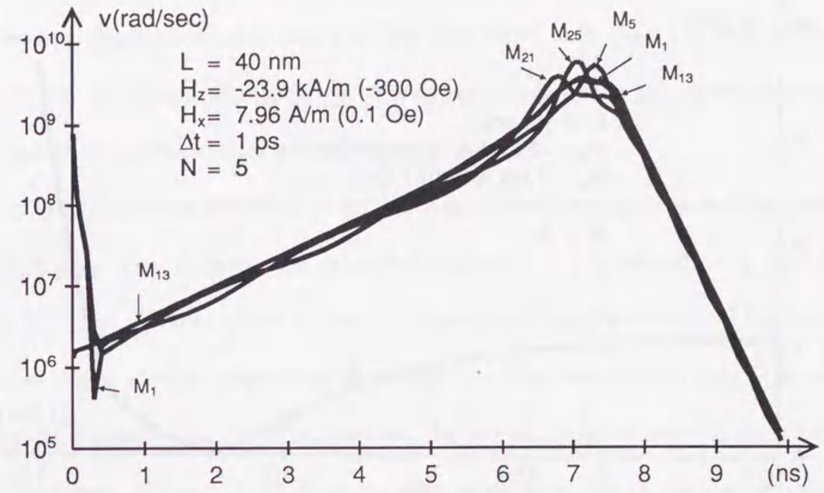

Figure 5.8: Change in the angular velocity in magnetization reversal from an F1 state.

among the five magnetizations in the F1 state.

The magnetization reversal mechanism in F1 state can be summarized as follows: just after the application of the external field, the z components of all the magnetic moments except for the moments in the particle center decrease to decrease the Zeeman energy. Because this transition increases the exchange energy, the transition terminates soon. Next, all of the moments start to precess in the same direction and at the same velocity. Any magnetic domain structure can not be seen in the cubic particle of F1 state because of its small size. The magnetizations should reverse coherently. But the magnetic moments point different directions in the flower state which is the equilibrium state of the cubic particle in the F1 state. Thus the reversal process cannot start just after the application of the external field. Figures 5.7(a) and 5.7(b) show that it takes about 6.5 ns until all the

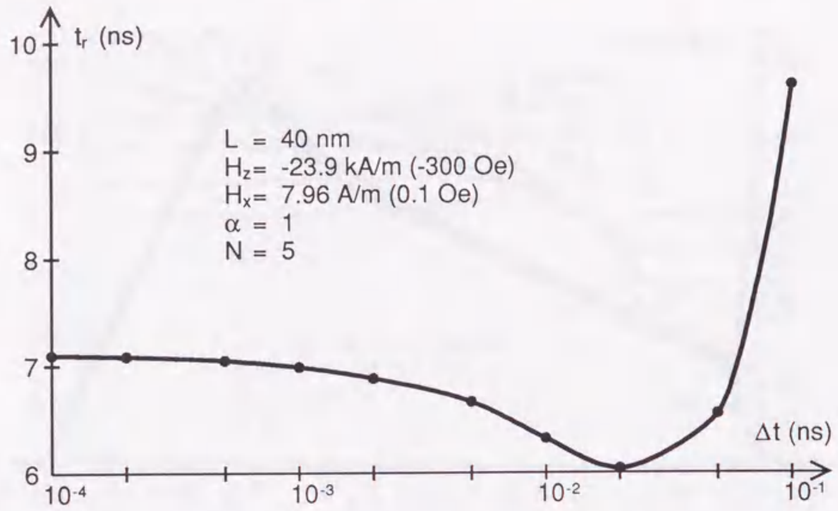

Figure 5.9: Effect of time step Δt on time interval τ_r.

moments are aligned in the same direction. Then the magnetization reversal starts.

5.4 Effect of Various Conditions on Magnetization Reversal

We have seen in the preceding section that in the magnetization reversal from the F1 state, a time τ_r is required before the irreversible transition occurs. In this section, the effect of the time step, offset field and damping factor on τ_r will be studied.

Effect of time step·

The effect of time step Δt on τ_r is shown in Fig. 5.9. When Δt is greater than 0.02 ns,

τ_r increases as Δt increases. When Δt is less than 0.02 ns, τ_r increases as Δt decreases. τ_r becomes constant when a time step less than 0.001 ns is used. In order to find the reason why τ_r changes with time step, the dynamic behavior of the center moment (M_{13} in Fig.5.6) on the top surface was examined.

Figure 5.10(a) shows the effect of the time step on the time dependence of the azimuthal angle of M_{13}. In this figure, the azimuthal angle at $t = 0$ is defined to be zero. When Δt is less than 0.020 ns which makes τ_r minimal, the time dependence of the azimuthal angle of M_{13} is almost independent of Δt until $t \doteq 8$ ns, which is the end of the reversal. When Δt is greater than 0.020 ns, however, the rate of change in azimuth angle decreases as Δt increases. Figure 5.10(b) shows the effect of the time step on the angular velocity of M_{13} ($|\dot{\boldsymbol{M}}_{13}|$). When Δt is greater than 0.020 ns, the angular acceleration of the moment decreases as Δt increases. On the other hand when Δt is less than 0.020 ns, the angular acceleration of the moment decreases as Δt decreases.

The effective gyroscopic and damping forces seem to decrease with increasing Δt when Δt is greater than 0.020 ns. This can be explained in the same manner as explained at the end of section 2.3.4: the Brown's equation is equivalent to the LLG equation in which the time derivatives of the magnetization angles are made to be zero, i.e., a very large time step is used. The effect of the gyroscopic and the damping torques will then disappear. On the other hand, when Δt is less than 0.020 ns, the gyroscopic and the damping forces seem to decrease as Δt decreases. It seems due to the discretization error.

Most calculation results shown in this section are derived from the time step as small as 0.001 ns. Then it seems that there is no advantage of using the implicit method to solve

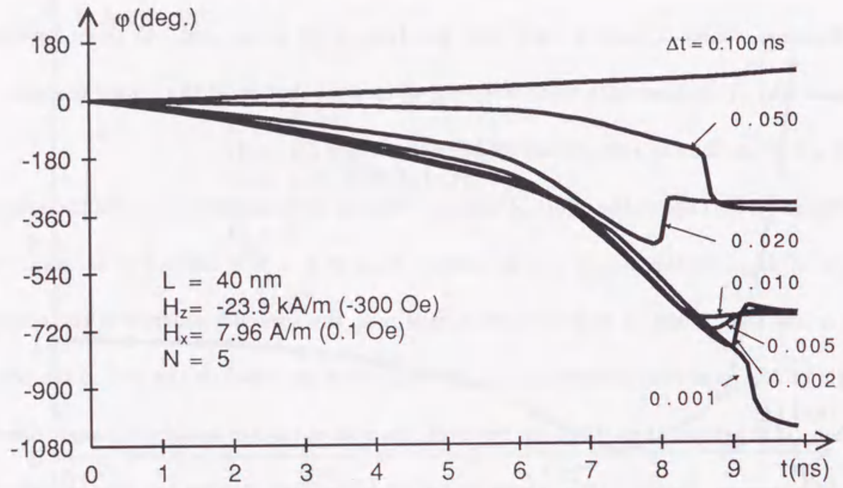

(a)

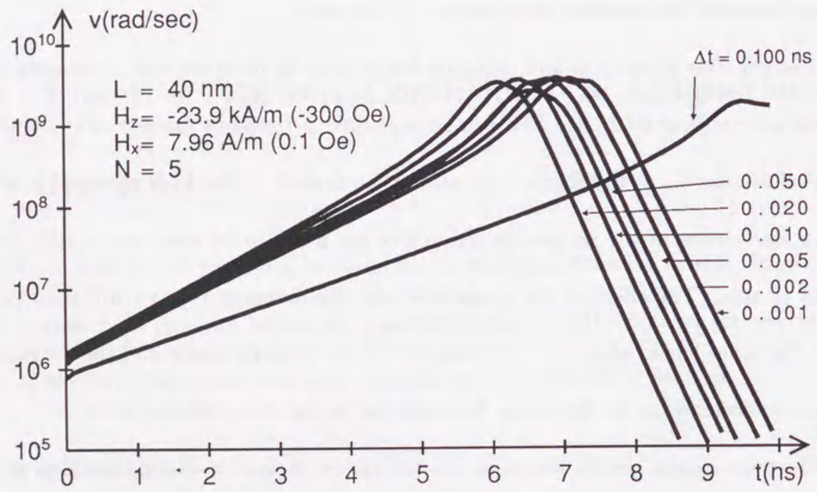

(b)

Figure 5.10: Effect of time step Δt on time dependence of magnetic moment at M_{13}. (a) Effect on the magnetization azimuth angle. (b) Effect on the angular velocity of the moment.

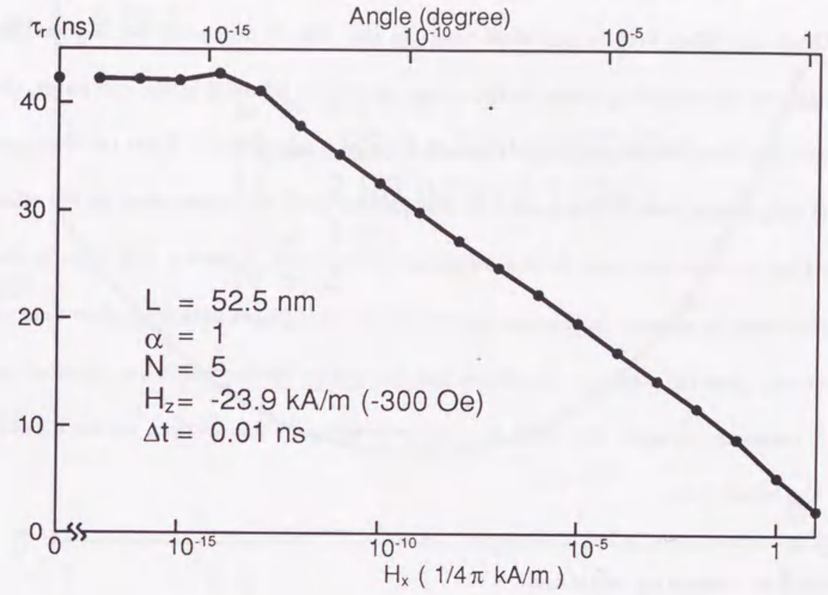

Figure 5.11: Effect of offset field H_x on time interval τ_r.

the LLG equation. But most micromagnetic calculations require a great deal of computing time. Thus some preliminary calculations with large time step are necessary even if we use much smaller time step in the final calculation. In such a case the methods which allow the use of large time steps are advantageous.

Effect of offset field

The effect of the offset field on τ_r is shown in Fig. 5.11. Here the magnitude of the applied field in the z direction was kept constant. τ_r increases with the decrease of the offset field until H_x is $1\times10^{-14}/4\pi$ kA/m. When the offset field is less than that value, τ_r becomes

constant. It is clear from symmetry consideration that the magnetizations cannot reverse without the offset field in the ideal case. In the case of numerical calculation, however, because of the rounding errors in the numerical values retained in the computer, the magnetization distribution may have chance to become asymmetric. Thus the demagnetizing field originating from this asymmetric distribution gives the same effect as the offset field. Because the rounding error by the computer is very small, it takes a long time for the effect of this error to appear. In this calculation the switching time with zero offset field does not have any physical meaning. To obtain the calculation results which has physical meaning, it is necessary to apply the offset field appropriately. In this section, we use $0.1/4\pi$ kA/m as the offset field.

Effect of damping constant

The dependence of τ_r on damping constant α is shown in Fig. 5.12. τ_r becomes minimum at $\alpha \approx 1$. When α is higher than unity, viscosity predominates over precession. As shown in the previous section, the magnetization of the 40-nm-size particle reverses almost coherently. It is shown analytically that τ_r is proportional to $(1+\alpha^2)/\alpha$ in the case of coherent rotation and τ_r takes a minimum at $\alpha = 1$ [58]. According to this theory, the τ_r of α=0.1 should coincide with the τ_r of α=10.0, but some discrepancy is seen in Fig. 5.12. It turns out that this difference is due to the numerical errors associated with the Δt which depend on α.

Fig. 5.13 shows the effect of the time step on τ_r in the cases with α= 0.1, 0.3, 1.0, 3.0 and 10.0. When α is greater than unity, τ_r does not depend on the time step significantly.

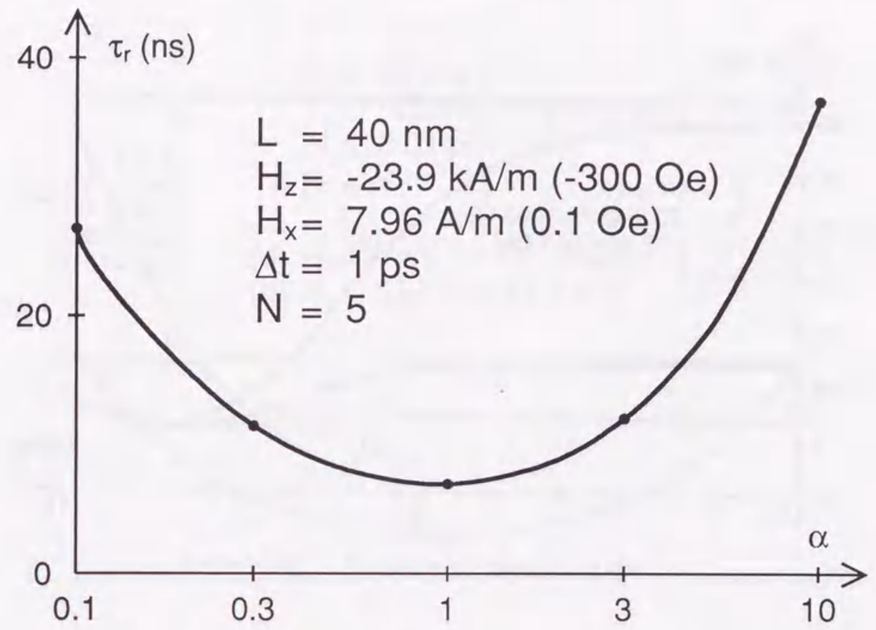

Figure 5.12: Effect of damping constant α on time interval τ_r.

When α is less than unity, however, τ_r depends strongly on the time step. Whereas τ_r becomes independent of Δt at Δt less than 0.1 ps is when α is 0.3, it is dependent on Δt while Δt is greater than 0.01 ps when α of 0.1 is used. From this figure, it is understood that we have to choose the time step depending on α.

Figure 5.14 shows the dependence of τ_r on damping constant when Δt of 0.01 ps is used. To compare this result with theory, we normalize τ_r with that at α of unity. The difference between the calculation value and the theoretical one is only 3.0% in the largest case. We also have made similar calculation using a larger offset field ($3.0/4\pi$ kA/m). In this case the difference between the calculation value and the theoretical one is 7.0% in the largest

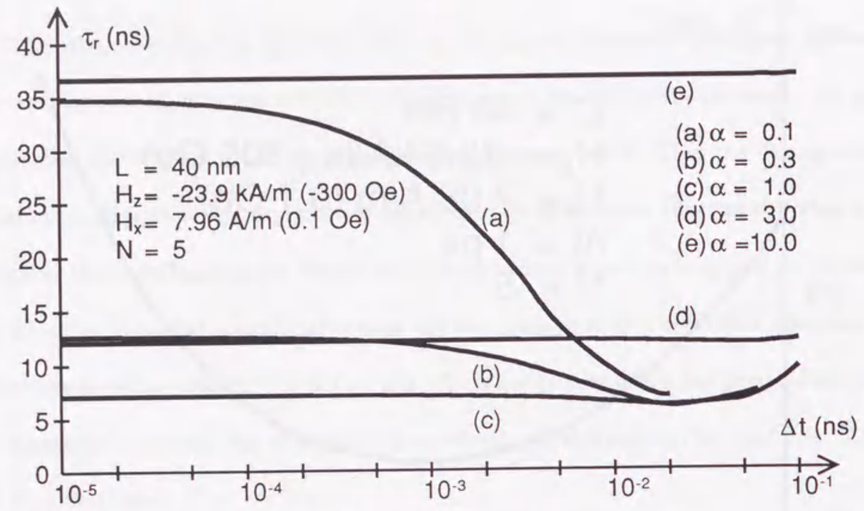

Figure 5.13: Effect of time step Δt on time interval τ_r.

case. It is expected that the deviation from theory will decrease with the decrease of the offset field.

In the remainder of chapter 5, the following calculation conditions are used considering the results shown above. The offset field is $0.1/4\pi$ kA/m, Δt is chosen less than 1 ps, and α is unity.

Effect of particle size

The effect of particle size on τ_r for the F1-state particle is shown in Fig. 5.15. τ_r becomes longer for larger particles.

Figure 5.16 shows the dependence of the angular velocity v of M_1 on the particle size L. The first peak in $v(L)$ curve, showing the maximum in $v(L)$, increases when the particle

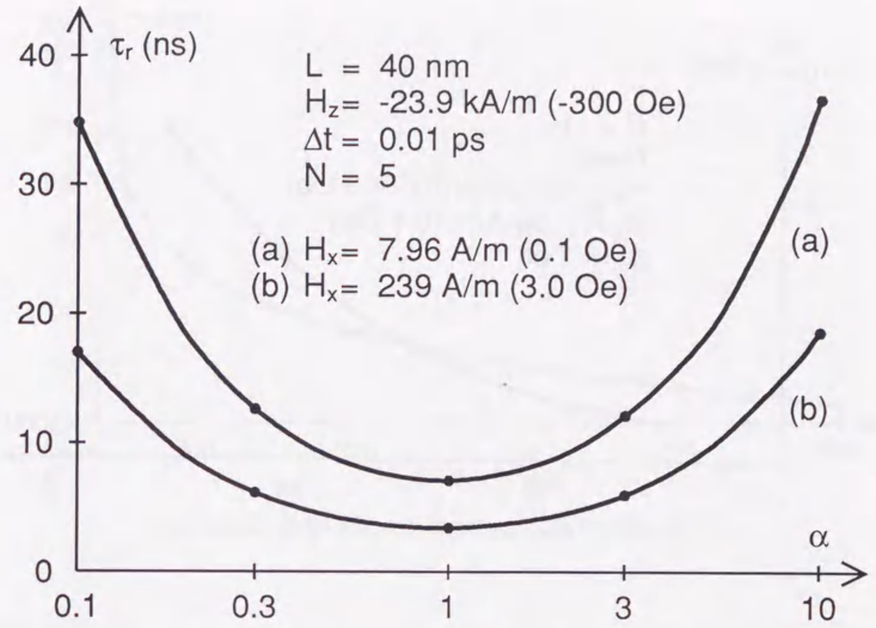

Figure 5.14: Effect of damping constant α on time interval τ_r.

size increases. The peak becomes broader as L increases.

Because the magnetization reversal mechanism from the F1 state is a coherent-like rotation, all moments align roughly to the same direction in the reversal period. Figure 5.16 shows that the initial rotational velocity of M_1 increases with particle size. τ_r is expected to increase with the increase of the displacement of the magnetization just after the application of the magnetic field. This initial displacement causes the misalignment of the magnetization. The magnetic moments of the cubic particle in the F1 state eventually reverse when all of the moments meet in the same direction. It becomes difficult for the moments to meet in the same direction with the increase of the initial displacements of the

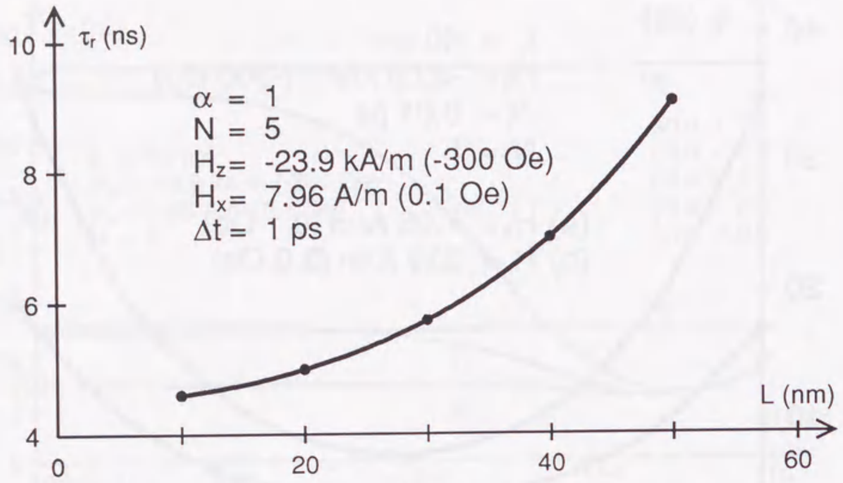

Figure 5.15: Dependence of time interval τ_r on particle size L.

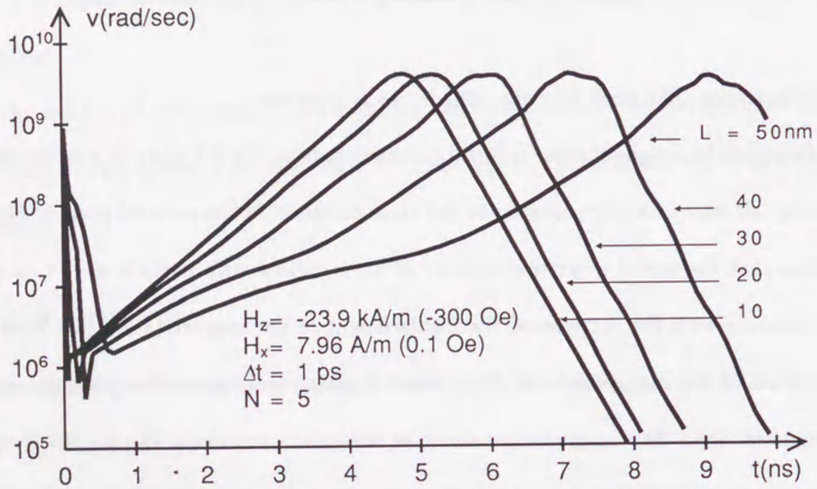

Figure 5.16: Dependence of the angular velocity of M_1 on particle size L.

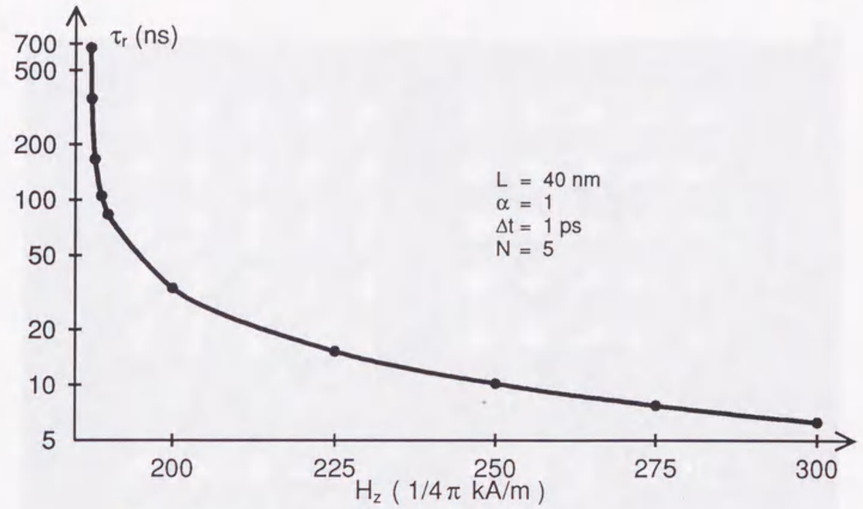

Figure 5.17: Dependence of time interval τ_r on reversing field H_z.

magnetizations.

The initial increases in the rotational velocities of the magnetic moments correspond to the increase in the retardation time τ_r with increasing particle size [7].

Effect of applied field

The time interval τ_r increases with decreasing applied field as shown in Fig. 5.17. At the switching field (H_{sw}), τ_r is expected to be infinite. This makes it difficult to determine the switching field exactly by computer simulation. Here the H_{sw} correspond to the H_c in Fig. 5.3.

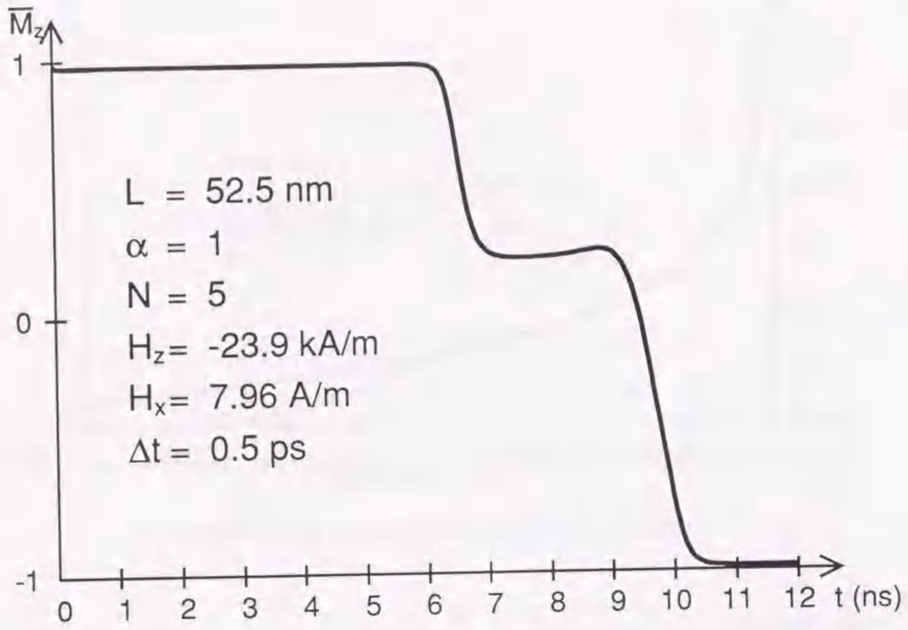

Figure 5.18: Change in $\overline{M}_z$ with time t for a 52.5-nm particle.

5.5 Magnetization Reversal from an F2 State

The switching mechanism of an F2 particle is different from that of an F1 particle. The change in $\overline{M}_z$ for a 52.5-nm particle with time is shown in Fig. 5.18. The magnetization is seen to reverse via two step transitions. There is an intermediate state between the two transitions.

The details of the magnetization reversal from an F2 state are shown in Fig. 5.19. The flower structure holds until the first transition begins (0~6 ns). When the first transition to the intermediate state begins, a vortex state appears (6~6.5 ns). In the intermediate (6.5~9

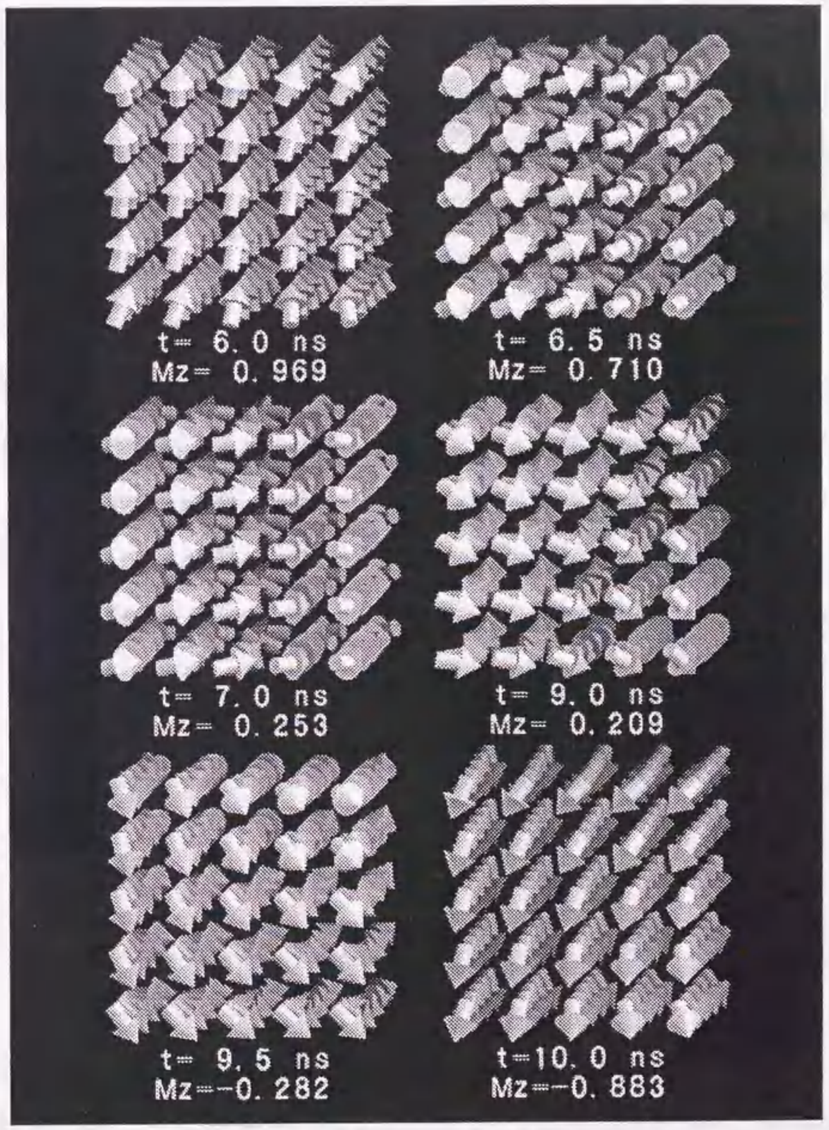

Figure 5.19: Mechanism of magnetization reversal from an F2 state.

ns) state the center of the vortex ($\theta = 0°$) is moving from the central part of the particle to the particle edge (rear xz plane in the figure). When the center of the vortex moves to the outside of the particle completely, the second transition begins. The magnetization reverses in coherent rotation mode (9-10.5ns), but the magnetization reversal is slow in the rear surface of the particle as compared with the front surface because the center of the vortex moves out from the rear surface of the particle.

Figure 5.20(a) shows the changes in the azimuthal angles of the five different moments on the top surface (Fig. 5.6). The azimuthal angle of M_{13} continues to decrease during the calculation. The other moments start rotation when the first transition occurs. All of the moments align to the same directions in the second transition except for M_{21}.

Figure 5.20(b) shows the changes in the polar angles of these five moments. The polar angle of M_{13} increases slightly until the first transition (t=0$\sim$7 ns), and then it increases monotonically. The polar angles of the other moments also change slightly until the first transition, but their motions become more complicated after the first transition. While the polar angle of M_1 which is the moment at the front left corner on the top layer almost increases continuously, the polar angles of M_5, M_{21} and M_{25} decrease in the second intermediate state. As mentioned above the center of the vortex disappears at the rear surface of the particle when the second transition starts. This is why the polar angles of these moments decrease in the second transition.

Figure 5.21 shows the angular velocity of the five moments on the top surface of the particle. Three peaks are observed: just after the application of the magnetic field and atthe first and the second transitions. The first peak was also observed in the case of F1

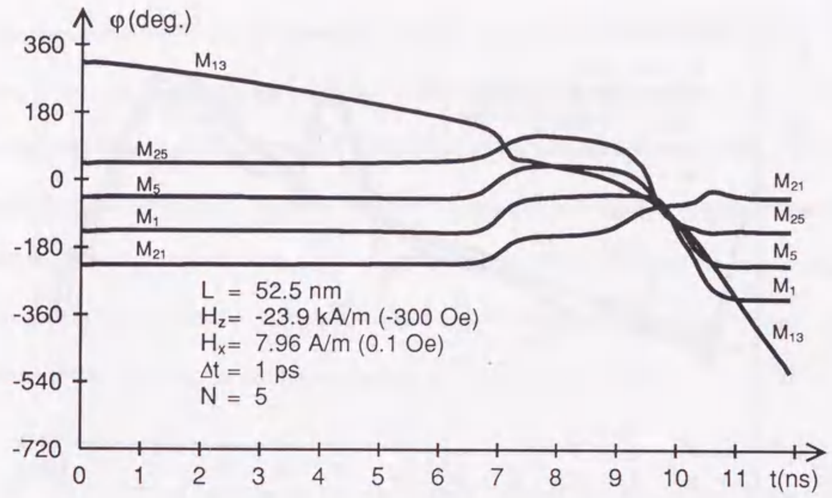

(a)

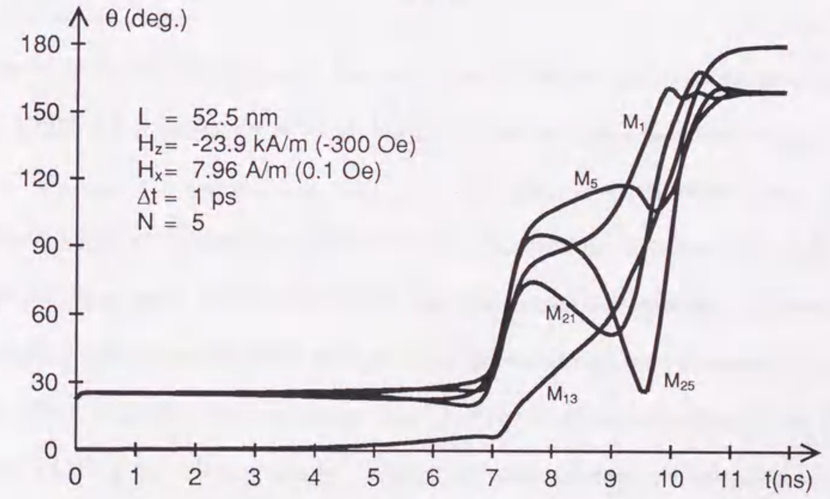

(b)

Figure 5.20: Time dependence of the magnetic moments in five different cells. (a) The changes in the azimuthal angles. (b) The changes in the polar angles.

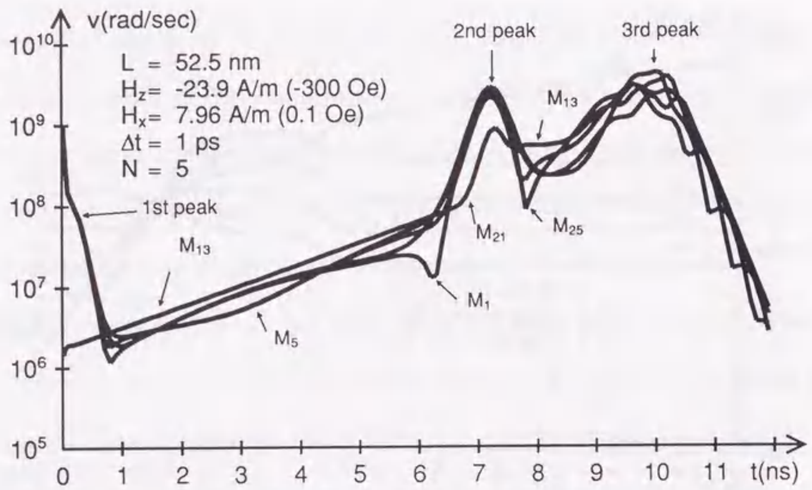

Figure 5.21: Change in the angular velocity with time in magnetization reversal from an F2 state.

state (Fig. 5.8), but the maximum velocity is larger and the width of the peak broader. It can be seen from this figure that the behavior of the five moments in the F2 state is almost the same as in the F1 state.

The mechanism of the magnetization reversal from the F2 state can be summarized as follows: the magnetization reverses with two kinds of transitions. There is an intermediate states between the two transitions. All of the magnetizations precess until the first transition occurs as the case in the F1 state. The vortex state appears after the first transition. Because the particle size is larger in the case of F2 state than in the case of the F1 state, the effect of the exchange energy is smaller. Thus less uniform magnetic structure like vortex is allowed to appear transiently in the particle of F2 state. But the size of the particle is not enough for the magnetization to reverse while keeping the vortex state. The magnetizations reverse in a coherent like mode in the second transition. In the intermediate state the center of the vortex is moving from the central part of the particle to the particle edge. When the size of the region in which the magnetic moments point the same direction exceeds beyond a critical value, the second transition occurs. (The particle of F2 state is larger than the particle of F1 state. It is not necessary that all of the magnetizations in the particle point the same direction.) Once the transition toward reversal starts, the magnetic moments in the rest of the particle also start the transition because they are coupled with the magnetic moments in the former region by the exchange energy.

5.6 Magnetization Reversal from a Vortex State

The magnetization reversal from a vortex state is shown in Fig. 5.22, where the change in $\overline{M}_z$ with time is summarized. It is seen from this figure that there are two kinds of transitions and an intermediate state. The first transition occurs just after the application of the magnetic field and the second transition does after the intermediate state.

The details of magnetization reversal from the vortex state is shown in Fig. 5.23. The first transition is a process in which the magnetic moment at the edge of the particle rotates to the applied field direction (0∼0.5 ns). In the intermediate state, the magnetization in the center of the vortex (in the central part of the particle) reverses slowly (0.5∼5.8 ns). The second transition occurs from the central part of the particle and spreads to the other parts (5.8-6.5 ns).

When magnetic fields smaller than the switching field are applied, the average magnetization, $\overline{M}_z$, decreases as shown in Fig. 5.3. The $\overline{M}_z$ returns to the original value when the

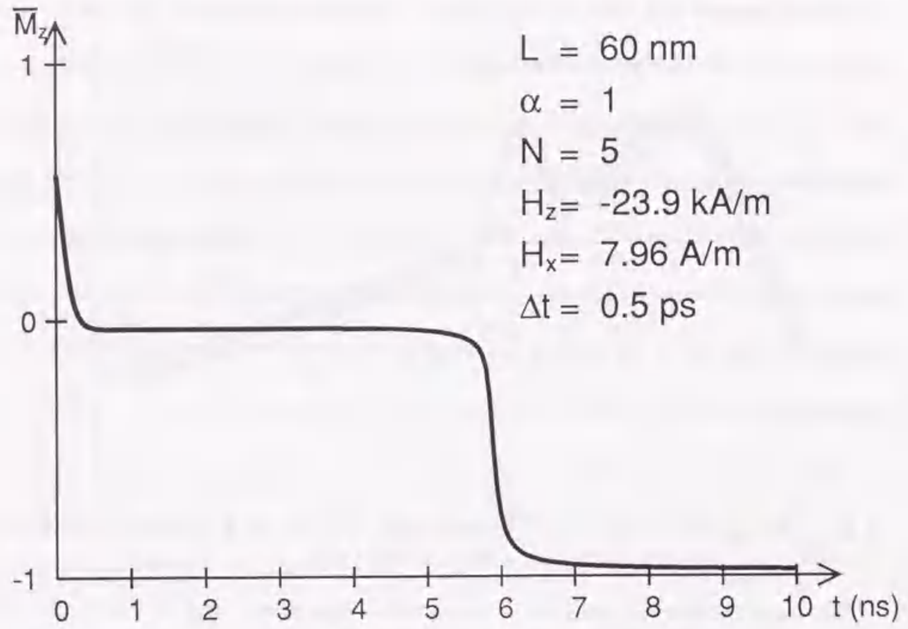

Figure 5.22: Change in $\overline{M}_z$ with time t for a 60 nm particle.

applied field is removed. This suggests that the first transition is a reversible process.

Figure 5.24(a) shows the changes in the azimuthal angles of the five moments on the top surface of the particle. The azimuthal angle of M_{13} continues to decrease during the calculation, making a peak at the second transition. But the azimuthal angles of the other moments do not change significantly. They remain almost constant except when the second transition occurs.

Figure 5.24(b) shows the changes in the polar angles of these moments. It can be seen from this figure that the motion of the moment at the center of the particle and those of the moments at the corners of the particle are quite different. The polar angle of the center

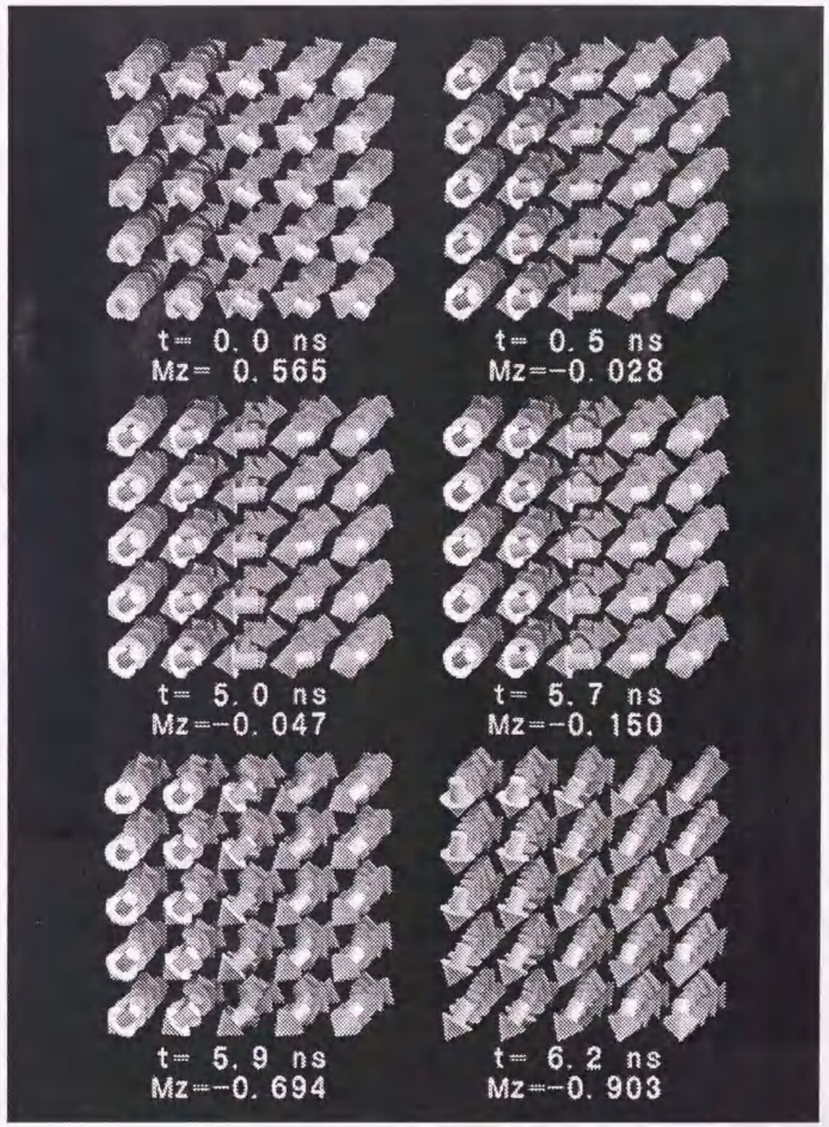

Figure 5.23: Mechanism of magnetization reversal from a vortex state.

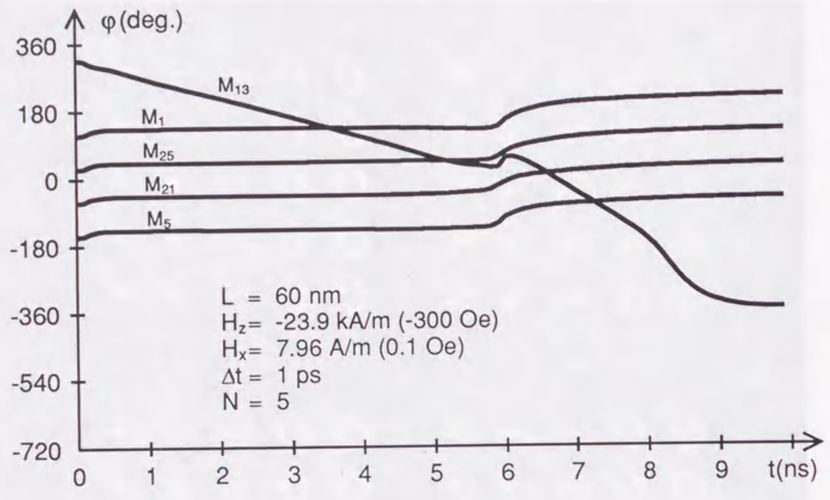

(a)

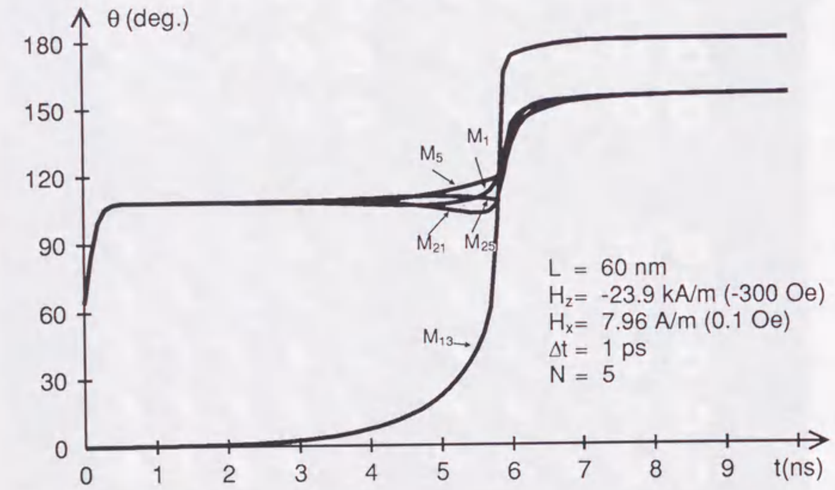

(b)

Figure 5.24: Time dependence of the magnetic moments in five top-surface cells in the magnetization reversal from a vortex state. (a) The changes in the azimuthal angles of the moments. (b) The changes in the polar angles of the moments.

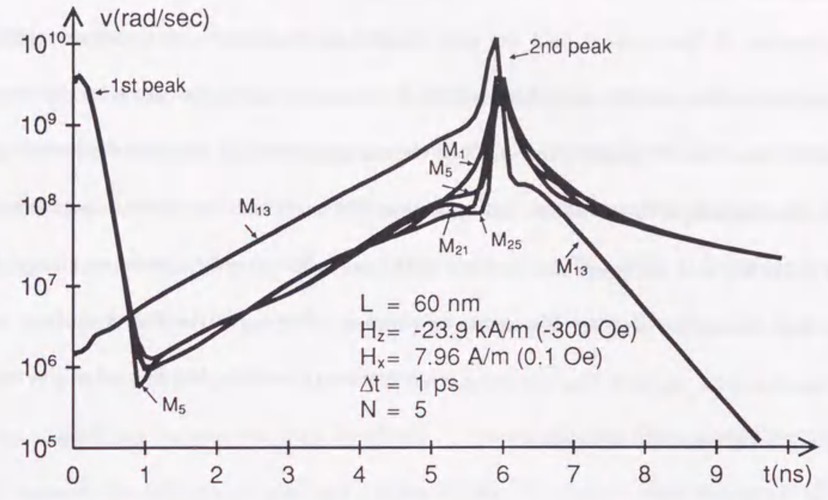

Figure 5.25: Change in the angular velocity in the magnetization reversal from a vortex state.

moment M_{13} increases slowly until the second transition occurs, and it increases rapidly at the second transition. On the other hand, there are two transitions in the polar angles of the other moments. These transitions correspond to the two transitions which were shown in Fig. 5.22.

Figure 5.25 shows the time dependence of the angular velocity of the five moments on the top surface of the particle. Two peaks are observed, corresponding to the two transitions shown in Fig. 5.22. The first peak is observed in the magnetization reversal from both F1 and F2 states (Fig. 5.8, Fig. 5.21), but the maximum velocity becomes higher and the width of the peak broader in the present case. The velocity of M_{13} is about 10 times as large as the velocity of the other moments in the intermediate state.

The mechanisms of the magnetization reversal from the vortex state can be summarized

as follows: there are two kinds of transitions and an intermediate state. Just after the application of the external field the polar angles of all magnetic moments except for the moments in the particle center increase (first transition). Because of the larger size of the particle than the F2 particle the effect of the exchange energy becomes decreased and the complicated magnetic structure can appear in the course of magnetization reversal. But the polar angle of the magnetic moment in the particle center M_{13} does not change during the first transition period. M_{13} starts to precess slowly after the first transition period. When the polar angle of M_{13} exceeds a critical value ($\theta \approx 60°$), M_{13} and all of the moments turn quickly (second transition).

5.7 Summary

The magnetization states and the details of the reversal process of the cubic particles derived by computer simulation are described in this section.

Two kinds of remanent states, flower and vortex, are found to exist depending on the particle size as reported by SB. In the intermediate particle sizes where the remanent state changes, two different states are found to exist depending on the initial state used in the calculation. The magnetization curves of the cubic particles of different sizes show that the flower state is further classified into two groups. The magnetization state of the smaller particle is termed the flower1 state and the other flower state found in the particles of intermediate sizes is distinguished as the flower2 state.

Magnetization reverses almost coherently in the irreversible transition from the flower1 state, though a time interval, τ_r, was necessary before the irreversible transition occurs. It

is found that the magnetic moments precessed around the reversing field and the angular velocities increased during this time interval.

The time interval τ_r was found to depend on the conditions such as the time step, offset field, damping constant, particle size, and applied field. It was found that τ_r varies with the time step, and that a considerably small time step is necessary so that we can obtain τ_r independent of time step. τ_r decreases with decreasing offset field. It becomes constant when the offset field is very small. τ_r becomes minimum when the damping constant is unity. τ_r increases with increasing particle size.

The magnetization reverses with two kinds of transitions and there is an intermediate state between the two transitions from a flower2 state. The vortex state appears in the first transition. The center of the vortex moves toward outside of the particle in the intermediate state. The magnetization reverses coherently in the second transition.

Two kinds of transitions and an intermediate state are observed in the magnetization reversal from a vortex state. The first transition is a process in which the magnetic moment at the edge of a particle rotates to the applied field direction. The magnetization in the central part of the particle reverses in the intermediate state. The second transition occurs from the central part of the particle and it spreads out to the other part.

Chapter 6

Conclusion

The numerical methods are proposed and developed to solve the problems in micromagnetics effectively using the Landau-Lifshitz-Gilbert (LLG) equation. Calculation results are presented showing the validity, capability, and usefulness of the derived methods. The methods are based on the backward-difference solution of the LLG equation so that the equation can be integrated with as large a time step as possible to reduce the computing time. The calculation results include detailed equilibrium magnetization structures such as three-dimension vertical Bloch lines in bubble-garnet films both with and without Bloch points (chapter 3), the cross-tie wall in a thin Permalloy film with cross-tie period of about one micrometer (chapter 4), and the two kinds of remanent magnetization structures, flower and vortex, in fine ferromagnetic particles of cubic shape (chapter 5). The results also include the time-dependent mechanisms of the magnetization reversal of the cubic particles which are found to occur in varieties of ways (chapter 5).

When one plans to construct numerical schemes for integrating the LLG equation, there

are two alternatives in the choice of the set of unknown variables which represent the magnetization, the magnetization angles and the Cartesian components of the magnetization. Numerical schemes based on the backward-difference method are constructed for the LLG equations expressed by both types of the unknowns variables. Both schemes, one for the LLG equation described by the magnetization angles and the other for the equation by the Cartesian components of the magnetization, are found almost equivalent with respect to the upper bound for the useful value of the time step though each scheme is found to have advantages and disadvantages.

The LLG equation expressed in the magnetization angles and discretized according to the backward-difference method satisfies the constraint of constant magnetization automatically. This eliminates the renormalization of the magnetization which is necessary in the case of the Cartesian-component representation after each time step, and makes the numerical scheme quite reliable. It is further found that the magnetization-angle representation yields less discretization error originating from the replacement of spatial derivatives by corresponding difference quotients (section 2.5). The magnetization-angle representation possesses a serious drawback of being unable to use when the polar angle of the magnetization has chance to reach zero or π. A novel method is proposed and implemented in which two kinds of coordinate frames are selected for each cell automatically within the framework of the backward-difference scheme (section 2.3). The calculation of the three-dimensional vertical Bloch lines, which is the largest-scale calculation so far made, has become possible owing to all these innovations.

The numerical scheme using the Cartesian components of the magnetization is attractive

in that it can be used for any kind of magnetization structure. However the LLG equation expressed by the Cartesian-components of the magnetization is found not to satisfy the constraint of constant magnetization if discretized straightforwardly. This is due to the presence of the expansion term, of the effective reversible torque, containing the expansion of the magnetization itself (section 2.4.3). It is found that this expansion term can be dropped without degrading the accuracy of the solution significantly so that the solution satisfies the constraint unconditionally. Owing to this modification, it becomes further possible to reduce the number of freedom from three to two per computing point by making use of the condition of constant magnetization (section 2.4.3). Thus the large-scale calculation for the cross-tie wall presented in chapter 4 becomes possible for the first time by the completion of the program based on the proposed numerical scheme. The size of the computing region is made as large (0.96 μm in the direction of the wall and 4.8 μm in the wall-normal direction) as the cost of computation permitted. The derived structure resembles the interference image of a cross-tie wall taken by electron holography closely, which shows the validity and effectiveness of the developed numerical scheme.

Before applying the proposed numerical schemes to actual problems of interest, the capability of the proposed methods are examined by one-dimensional calculations, in which an initial magnetization structure given appropriately for thin Permalloy film is relaxed to the Bloch structure (section 2.5). It is found that the LLG equations discretized according to the backward-difference method can be solved using time steps 5 to 700 times as large as those for equations discretized according to the conventional forward-difference method depending on the calculation condition, whether the equations are represented by the

magnetization angles or the Cartesian-components of the magnetization. While the largest usable time step is proportional to $\alpha\delta x^2$ if the forward-difference method is used, the largest usable time step in the case of the backward-difference method is found to depend on neither α nor δx significantly.

In the two-dimensional calculation of the vertical Bloch line presented in chapter 3, the magnetization structures of a plane-like wall are calculated with either vertical Bloch lines of same winding polarities or magnetostatically coupled vertical Bloch line pairs spaced periodically. The results of the calculation reveal the detailed structures of the two-dimensional wall which so far had been known only conceptually on the basis of approximate theory. It is found that the wall has not only its thickness constricted in the neighborhood of a vertical Bloch line but also its shape is deformed to decrease the magnetostatic energy.

In chapter 3, the magnetization structures of vertical Bloch lines and Bloch points are derived in the three-dimensional calculation, where the computing region is extended so that the results of computation can be compared with experiment directly. The derived three-dimensional structure of a vertical Bloch line shows a new feature that the wall tilts around the Bloch line center, the fact which had been expected experimentally but can not be derived by two dimensional calculation. The results of computation, in which both the amount of wall tilt and the width of wall microdeformation are included, agree with the experimentally observed values. The calculation shows that a wall containing a Bloch point tilts by the same amount as the wall without Bloch points. This suggests that a composite Bloch line which contains a Bloch point can also be observed optically though it may be difficult to distinguish a composite Bloch line from a simple Bloch line.

In chapter 5, the magnetization states and the reversal mechanisms of the cubic particles are investigated utilizing the ability of the developed scheme to solve dynamic problems. Two kinds of magnetization states, flower and vortex, are found to exist depending on the particle size. At the transient particle size where the equilibrium state changes, different states are derived depending on the initial state used. The magnetization curves of the cubic particles of different sizes show that the flower state is further divided into two groups depending on the particle size near the transient. The magnetization state of smaller particle size is termed the flower1 state and that of the particle with a size near the transient is termed flower2 state in this thesis.

Magnetization reverses almost coherently in the irreversible transition from the flower1 state. Some time interval τ_r, however, is required before the irreversible magnetic transition occurs. During this interval, the magnetic moments continuous to precess and the angular velocity is increasing until the transition occurs. The time interval, τ_r, is found to depend on the conditions such as offset field, damping constant, particle size, and applied field. τ_r is found to decrease with decreasing offset field. It becomes constant when the latter is decreased less than a critical value. It is also found that τ_r varies with the time step, and that a considerably small time step is required to obtain τ_r independent of time step. As for the dependence of τ_r on the damping constant α, τ_r is found to become minimum when α=1. τ_r is found to increase with increasing particle size.

In the magnetization reversal from the flower2 state, the magnetization is reverse by two steps of transitions with an intermediate state between them. The vortex state appears in the first transition, then the center of the vortex moves towards outside of the particle in

the intermediate state. The magnetization reverses coherently in the second transition.

Two kinds of transitions and an intermediate state are also observed in the magnetization reversal from the vortex state. The first transition is found to be a process in which the magnetic moment at the edge of a particle rotates to the applied field direction. The magnetization in the central part of the particle reverses in the intermediate state. The second transition occurs from the central part of the particle and it spread out to the other part.

References

[1] William Fuller Brown, Jr.,. *Micromagnetics*. Interscience Publishers, New York, 1963.

[2] A. E. Labonte and Wiliam Fuller Brown, Jr. One-dimensional zero-degree double Bloch walls in thin films. *Journal of Applied Physics*, vol. **37**(3):1299, March 1966.

[3] A. E. Labonte. Two-dimensional Bloch-type domain walls in ferromagnetic films. *Journal of Applied Physics*, vol. **40**(6):2450, May 1969.

[4] Alex Hubert. Stray-field-free magnetization configurations. *Phys. Stat. Solidi*, vol. **32**:519, 1969.

[5] Alex Hubert. Stray-field-free and related domain wall configurations in thin magnetic films (II). *Phys. Stat. Solidi*, vol. **38**:699, 1970.

[6] M. E. Schabes and A. Aharoni. Magnetostatic interaction fields for a three-dimensional array of ferromagnetic cubes. *IEEE Transactions on Magnetics*, vol. **MAG-23**(6):3882, November 1987.

[7] M. E. Schabes and H. N. Bertram. Magnetization processes in ferromagnetic cubes. *Journal of Applied Physics*, vol. **64**(3):1347, August 1988.

[8] Randall H. Victora. Micromagnetic predictions for barium ferrite particles. *Journal of Applied Physics*, vol. **63**(8):3423, April 1988.

[9] E. Della Torre. Fine particle micromagnetics. *IEEE Transactions on Magnetics*, vol. **MAG-21**(5):1423, September 1985.

[10] E. Della Torre. Magnetization calculation of fine particles. *IEEE Transactions on Magnetics*, vol. **MAG-22**(5):489, September 1986.

[11] Ying Dong Yan and Edward Della Torre. Modeling of elongated fine ferromagnetic particles. *Journal of Applied Physics*, vol. **66**(1):320, July 1989.

[12] M. Mansuripur. Magnetization reversal dynamics in the media of magneto-optical recording. *Journal of Applied Physics*, vol. **63**(12):5809, June 1988.

[13] Susumu Konishi. A new ultra-high-density solid state memory: Bloch line memory. *IEEE Transactions on Magnetics*, vol. **MAG-19**(5):1838, September 1983.

[14] Nobuo Hayashi and Yoshinobu Nakatani. A lumped-constant model of vertical Bloch lines. *Journal of the Magnetic Society of Japan*, vol. **9**(2):181, 1985.

[15] Nobuo Hayashi and Yoshinobu Nakatani. Computer simulation of magnetic domain wall motion to derive effective interaction forces between vertical Bloch lines. *IEEE Transactions on Magnetics*, vol. **MAG-22**(5):796, September 1986.

[16] Nobuo Hayashi and Yoshinobu Nakatani. Numerical calculation of magnetic bubble domain wall motion based on a lumped-constant model of vertical Bloch lines. *Japanese Journal of Applied Physics*, vol. **25**(3):406, March 1986.

[17] Yoshinobu Nakatani and Nobuo Hayashi. Variational calculus for vertical Bloch lines. *Journal of the Magnetic Society of Japan*, vol. **11**(2):133, 1987.

[18] Kimihide Matsuyama and Susumu Konishi. Computer simulation of domain wall and vertical Bloch line motion in a bubble garnet film. *IEEE Transactions on Magnetics*, vol. **MAG-20**(6):1141, November 1984.

[19] G. Ronan, Kimihide Matsuyama, E. Fujita, M. Ohbo, and Susumu Konishi. Three-dimensional computer model of domain wall motion in magnetic bubble materials. *IEEE Transactions on Magnetics*, vol. **MAG-21**(6):2680, November 1985.

[20] Motoko Hasegawa, Hisao Matsutera, K. Moroga, and Yasuharu Hidaka. Three dimensional computer simulation of vertical Bloch line motion in a Bloch line memory. *IEEE Transactions on Magnetics*, vol. **MAG-22**(5):802, September 1986.

[21] A. Thiaville, L. Arnaud, F. Boileau, G. Sauron, and J. Miltat. Direct Bloch line optical observation (invited). *Journal of Applied Physics*, vol. **63**:3153, 1988.

[22] A. Thiaville, J. Ben Youssef, Y. Nakatani, and J. Miltat. On the influence of wall microdeformations on Bloch line visibility in bubble garnets (invited). *Journal of Applied Physics*, vol. **69**(8):6090, April 1991.

[23] C. Kooy and U. Enz. Experimental and theoretical study of the domain configuration in thin layers of $BaFe_{12}O_{19}$. *Phillips Res. Repts.*, vol. **15**:7, 1960.

[24] J. C. Slonczewski. Properties of Bloch points in bubble domains. *AIP conf. Proc.*, vol. **24**:613, 1975.

[25] A. P. Malozemoff and J. C. Slonczewski. *Magnetic Domain Wall in Bubble Materials.* Academic Press, New York, 1979.

[26] E. Feldtkeller. Mikromagnetisch stetige und unstetige Magnetisierungskonfigurationen. *Z. Angew. Phys.*, vol. **19**:530, 1965.

[27] T. Obokata, K. Yamaguchi, and K. Asama. Temperature stability of bubble domain wall states. *AIP Conf. Proc.*, vol. **29**:74, 1976.

[28] J. C. Slonczewski. Theory of Bloch-line and Bloch-wall motion. *Journal of Applied Physics*, vol. **45**:2705, 1974.

[29] Nobuo Hayashi and Koki Abe. Computer simulation of magnetic bubble domain wall motion. *Japanese Journal of Applied Physics*, vol. **15**(9):1685, September 1976.

[30] Nobuo Hayashi and Hirohide Mikami. Computer simulation of magnetic bubble domain Bloch lines motion. *Japanese Journal of Applied Physics*, vol. **19**(2):295, February 1980.

[31] B. MacNeal and F. Humphrey. Horizontal Bloch line motion in magnetic bubble materials. *IEEE Transactions on Magnetics*, vol. **MAG-15**(5):1272, September 1979.

[32] S. Speidel, H. Yamakawa, S. Iwata, and S. Uchiyama. Simulation of Bloch wall motion in bubble films. *IEEE Transactions on Magnetics*, vol. **MAG-20**(5):1147, September 1984.

[33] C. C. Shir. Computations of the micromagnetics in domain walls. *Journal of Applied Physics*, vol. **49**(6):3413, June 1978.

[34] F. Bloch. Zur Theorie Des Austauschproblems und der Remanenzerscheinung der Ferromagnetika. *Z. f. Phys.*, vol. **74**:295, 1932.

[35] L. Neel. *Compt. Rend.*, vol. **241**:533, 1955.

[36] E. E. Huber, D. O. Smith, and J. B. Goodenough. Domain-wall structure in Permalloy films. *Journal of Applied Physics*, vol. **29**:294, 1958.

[37] S. Middelhock. Domain walls in thin Ni-Fe films. *Journal of Applied Physics*, vol. **34**(4):1054, April 1963.

[38] Takao Suzuki. Asymmertric 180° Bloch walls in Fe single crystal films. *Japanese Journal of Applied Physics*, vol. **17**(1):141, January 1978.

[39] Akira Tonomura, Tsuyoshi Matsuda, Hideo Tanabe, Nobuyuki Osakabe, Junji Endo, Akira Fukuhara, Kohsei Shinagawa, and Hideo Fujiwara. Electron holography technique for investigating thin ferromagnetic films. *Phys. Rev. B*, vol. **25**(11):6799, June 1982.

[40] E. C. Stoner and E. P. Wohlfarth. A mechanism of magnetic hysteresis in heterogeneous alloys. *Philosophical Transaction of the Royal Society of London*, vol. **A240**:599, 1948.

[41] I. S. Jacobs and C. P. Bean. An approach to elongated fine-particle magnets. *Physical Review*, vol. **100**(4):1060, November 1955.

[42] S. Shtrikman E. H. Frei and F. Treves. Critical size and nucleation field of ideal ferromagnetic particles. *Physical Review*, vol. **106**(3):446, May 1957.

[43] A. Aharoni and S. Shtrikman. Magnetization curve of the infinite cylinder. *Physical Review*, vol. **109**(5):1522, March 1958.

[44] S. Shtrikman and D. Treves. The coercive force and rotational hysteresis of elongated ferromagnetic particles. *Le Journal de Physique et le Radium*, (20):286, February-March 1959.

[45] William Fuller Brown, Jr. Criterion for uniform micromagnetization. *Physical Review*, vol. **105**(5):1479, March 1957.

[46] Amikan Aharoni. Some recent developments in micromagnetics at the Weizmann institute of science. *Journal of Applied Physics*, vol. **30**(4):70, April 1959.

[47] Fred E. Luborsky. High coercive materials development of elongated particle magnets. *Journal of Applied Physics*, vol. **32**(8):171, March 1961.

[48] J. E. Knowles. Magnetic properties of individual acicular particles. *IEEE Transactions on Magnetics*, vol. **MAG-17**(6):3008, November 1981.

[49] J. E. Knowles. The measurement of the anisotropy field of single tape particle. *IEEE Transactions on Magnetics*, vol. **MAG-20**(1):84, January 1984.

[50] A. R. Corradi, S. J. Andress, J. E. French, G. Bottoni, D. Candolfo, A. Cecchetti, and F. Masoli. Magnetic properties of new (np) hydrothermal particles. *IEEE Transactions on Magnetics*, vol. **MAG-20**(1):33, January 1984.

[51] A. E. Berkowitz. Some materials considerations in particulate media. *IEEE Transactions on Magnetics*, vol. **MAG-22**(5):466, September 1986.

[52] Gordon D. Smith. *Numerical Solution of Partial Differential Equations.* Oxford University Press, 1965.

[53] R. Flecher. Conjugate gradient methods for indefinite systems, in G. A. Watson, editor, numerical analysis dundee 1975. In *Lecture Note in Math. 506*, pages 73–89, Springer-Verlarg, New York, 1976.

[54] H. Chang. Analysis of static and quasidynamic behavior of magnetostatically coupled thin magnetic films. *IBM J. Res. & Develop.*, vol. **6**:419, 1962.

[55] Wiliam Fuller Brown, Jr and A. E. Labonte. Structure and energy of one-dimensional domain walls in ferromagnetic thin films. *Journal of Applied Physics*, vol. **36**(4):1380, April 1965.

[56] P. Sonneveld. Cgs, a fast lanczos-type solver for nonsymmetric linear systems. *Rep. 84-16, Delft Univ., Dept. of Math., Delft, The Netherlands.*, 1984.

[57] J. K. Galt. Motion of individual domain walls in a Nickel-Iron ferrite. *Bell Syst. Tech. J.*, vol. **33**:1023, 1954.

[58] Soshin Chikazumi. *Physics of Ferromagnetism.* John Wiley and Sons, Inc., New York, 1964.